PHILOSOPHICAL TRANSACTIONS A

royalsocietypublishing.org/journal/rsta

Review

Cite this article: Aumann T, Bertulani CA, Duer M, Galatyuk T, Obertelli A, Panin V, Rodríguez-Sánchez JL, Roth R, Stroth J. 2024 Nuclear structure opportunities with GeV radioactive beams at FAIR. *Phil. Trans. R. Soc. A* **382**: 20230121.
https://doi.org/10.1098/rsta.2023.0121

Received: 19 October 2023
Accepted: 10 April 2024

One contribution of 11 to a theme issue 'The liminal position of Nuclear Physics: from hadrons to neutron stars'.

Subject Areas:
nuclear physics

Keywords:
rare isotopes, radioactive beams, FAIR, R^3B

Author for correspondence:
M. Duer
e-mail: mduer@ikp.tu-darmstadt.de

Nuclear structure opportunities with GeV radioactive beams at FAIR

T. Aumann[1,2,3], C. A. Bertulani[3,4], M. Duer[1], T. Galatyuk[1,2,3], A. Obertelli[1,3], V. Panin[2], J. L. Rodríguez-Sánchez[5], R. Roth[1,3] and J. Stroth[2,3,6]

[1]Institut für Kernphysik, Technische Universität Darmstadt, Darmstadt 64289, Germany
[2]GSI Helmholtzzentrum für Schwerionenforschung GmbH, Planckstraße 1, Darmstadt 64291, Germany
[3]Helmholtz Forschungsakademie Hessen für FAIR (HFHF), Darmstadt 64291, Germany
[4]Texas A&M University-Commerce, Commerce, TX 75429, USA
[5]CITENI, Campus Industrial de Ferrol, Universidade da Coruña, Ferrol 15403, Spain
[6]Institut für Kernphysik, Johann Wolfgang Goethe-Universität, Frankfurt 60438, Germany

RR, 0000-0003-4991-712X

The Facility for Antiproton and Ion Research (FAIR) is in its final construction stage next to the campus of the Gesellschaft für Schwerionenforschung Helmholtzzentrum for heavy-ion research in Darmstadt, Germany. Once it starts its operation, it will be the main nuclear physics research facility in many basic sciences and their applications in Europe for the coming decades. Owing to the ability of the new fragment separator, Super-FRagment Separator, to produce high-intensity radioactive ion beams in the energy range up to about 2 GeV/nucleon, these can be used in various nuclear reactions. This opens a unique opportunity for various nuclear structure studies across a range of fields and scales: from low-energy physics via the investigation of multi-neutron systems and halos to high-density nuclear matter and the equation of state, following heavy-ion collisions, fission and study of short-range correlations in nuclei and hypernuclei. The newly developed reactions with relativistic radioactive beams (R^3B) set up at FAIR would be the most suitable and versatile for such studies. An overview

THE ROYAL SOCIETY PUBLISHING

royalsocietypublishing.org/journal/rsta Phil. Trans. R. Soc. A 382: 20230121

of highlighted physics cases foreseen at R^{3}B is given, along with possible future opportunities, at FAIR.

This article is part of the theme issue 'The liminal position of Nuclear Physics: from hadrons to neutron stars'.

1. Introduction

A main frontier in nuclear structure studies today is the physics of radioactive ion beams. About 300 stable or long-lived isotopes can be found in nature. These tightly bound nuclei are located at the valley of stability. By adding neutrons or protons to (or equivalently removing protons or neutrons from) them, one moves to unstable, short-lived radioactive isotopes, until reaching the limit of existence of nuclear binding, the neutron and proton drip lines. Beyond the drip lines, the nuclear interaction cannot bind additional neutrons or protons to a nucleus, and the systems are unstable against the emission of nucleons.

As most of the short-lived isotopes do not exist on earth, they have to be synthesized from stable nuclei, most often accelerated in an ion state, and studied just after production, before radioactive decay, e.g. by β-decay, α-decay or fission. Owing to the developments of new-generation radioactive ion beam (RIB) facilities worldwide, a broad range of short-lived isotopes have been produced, including those with extreme neutron-to-proton ratios. As of today, about half of the predicted exotic nuclei are still unexplored owing to experimental challenges in their production. The proton drip line is well-established up to a high atomic number ($Z = 93$) [1], since it is located closer to stability owing to the Coulomb interaction. The neutron drip line, on the other hand, is located further away from the valley of stability and is currently known only up to neon ($Z = 10$) at ^{34}Ne [2], 12 neutrons away from stability. RIBs, at a wide range of nuclear species and energies, offer a unique possibility to access many aspects of the nuclear many-body problem as well as prospects for exotic structure phenomena not observed in stable nuclei. The occurrence of new features is related to the large isospin asymmetry in these nuclei and their low-binding energy, thus the vicinity to the continuum.

In the last few decades, experiments with RIB have revealed a variety of new nuclear phenomena. The shell evolution of extremely neutron-rich nuclei appears to have a different structure than the traditional one of stable nuclei, where known-so-far magic numbers disappear while new ones emerge in different regions of the nuclear chart [3]. Far from stability, at the edge of the neutron drip line, where valence neutrons are loosely bound, halo effects appear, and the neutron wave function extends far beyond the typical radius of the nucleus. The studies of halo nuclei were initiated in the mid-80s from interaction cross-section measurements of light neutron-rich nuclei [4], where high-energy radioactive beams have first been used for nuclear reactions. The unexpectedly large matter radius of ^{11}Li was interpreted as a system composed of a ^{9}Li core with two neutrons whose wave functions extend through quantum tunnelling to a region of space that is classically forbidden [5]. Meanwhile, several halo nuclei have been identified and characterized with weakly bound *s*- or *p*-wave neutrons. Complementary observables have been used from direct reactions and spectroscopy after neutron transfer, knockout or Coulomb excitation, charge radii from isotopic shifts and matter radii from elastic scattering. For heavier nuclei, neutron skins develop, corresponding to a neutron density higher than that of the proton at the nuclear surface.

Of particular interest are two-neutron halo nuclei, where correlations among the neutrons play an essential role. Loosely spaced Bardeen–Cooper–Schrieffer pairing correlation between two nucleons is known to stabilize nuclei. On the other hand, in neutron-rich nuclei in the region of low density, a compact space correlation is expected to appear, the di-neutron correlation. Two-neutron Borromean nuclei are well suited to study this low-density correlation. Di-neutron correlation has been evidenced in such Borromean nuclei near the neutron

royalsocietypublishing.org/journal/rsta Phil. Trans. R. Soc. A 382: 20230121

drip line, suggesting it to be a universal feature [6]. At extreme neutron-to-proton asymmetry beyond the neutron drip line, the neutron–neutron (*NN*) correlations are of great importance. The most neutron-rich systems are unbound neutron states beyond the drip line, where neutron cluster emission is expected. For example, two-neutron emission from unbound ^{10}He or ^{26}O and possibly the occurrence of heavier multi-neutron clusters.

Nuclear reactions are essential to address the physics at the limit of stability. In particular, a powerful method applied to radioactive beams is quasifree scattering (QFS), which is well-established as a spectroscopic tool for nuclear structures [7]. Moreover, QFS nucleon knock-out reactions in inverse kinematics offer a new and unique approach for fission studies [8,9]. The fissioning nuclei induced by, e.g. $(p, 2pf)$ reactions (f the fission fragments) can be fully characterized in terms of their excitation energy.

Nuclear physics has an enormous impact on astrophysics, from the microscopic properties of neutron stars to the nucleosynthesis of heavy elements. In particular, neutron-rich matter at very low densities provides insight into the physics at the inner crust of neutron stars, where the density is smaller than the nuclear saturation density, ρ_0, $10^{-4} \lesssim \rho/\rho_0 \lesssim 0.5$. In such low densities, the large *s*-wave scattering length of the *NN* interaction dominates. At intermediate nuclear densities, it guides and constrains the physics of neutron-rich nuclei, which are key for understanding nucleosynthesis. At higher densities that exceed several saturation densities, such as those reached in the core of neutron stars, the state of nuclear matter is still unknown. At these high densities, exotic states of matter containing strange quarks, hyperons, correlated quark matter or quark-gluon plasma can emerge [10]. As such, neutron stars are also a testing ground for two- and few-body hadronic interactions.

A worldwide effort has developed in the last two decades to study nuclear matter over a wide density range and isospin asymmetry, both experimentally and theoretically. A key ingredient for modelling such dense matter is the equation of state (EOS), i.e. the thermodynamical properties of matter under extreme conditions of density, temperature, gravity and isospin, which depends strongly on the constituents of the matter and the interactions among them. A precise knowledge of the EOS is essential for assessing the physics of neutron stars, mergers, supernova explosions and the nucleosynthesis of heavy elements.

Nuclear structure studies address the region around saturation density and give precious information to constrain the nuclear EOS, which can be extrapolated up to $2\rho_0$ using an extrapolation by using effective field theory (EFT) and interactions calibrated around ρ_0, thus overlapping with constraints from heavy-ion collisions (see below). Nuclear ground-state properties and nuclear excitations carry information on the symmetry energy, which relates between pure neutron matter and symmetric nuclear matter, and the neutron pressure at around nuclear saturation density (see [11] for a review). Experimental methods to determine the electric dipole polarizability and neutron-skin thickness of neutron-rich nuclei, both constraining the neutron pressure around saturation density and zero temperature, have been developed recently [12,13]. Most of the relevant densities in the inner region of neutron stars, however, are not accessible at laboratory experiments, and experimental constrains on the properties of neutron-rich matter are still very scarce.

Understanding the properties of high-density nuclear matter would benefit from the microscopic description of short-range correlated (SRC) nucleons in the nuclear ground-state wave function, governed by the fundamental nucleon–nucleon (*NN*) interaction at short distances. At relativistic energies of around 1.5 GeV/nucleon, densities up to $3\rho_0$ can also be reached by colliding two energetic heavy nuclei against each other, e.g. Au + Au [14]. In this way, the different phases of matter under extreme conditions of temperature and density may be investigated. Finally, the inner composition of neutron stars remains an open question. At high densities, strange nuclear matter is expected to be stable [15–17], leading to a significant fraction of strange quarks in the form of kaons and hyperons. Those will influence the EOS, e.g. their presence will soften it, following the hyperon–nucleon (YN) interactions and interactions

involving hyperons in general, all of which are poorly constrained nowadays owing to lack of experimental data. The YN interactions can be investigated via spectroscopy of short-lived hypernuclei, although the experimental data are very limited so far [18], in particular for neutron-rich hypernuclei that could provide key information related to strangeness in dense neutron-rich matter. Measurements of the binding energy of new hypernuclei will allow us to constrain the YN interactions and derive an EOS with variable isospin and strangeness up to ~$2\rho_0$. On the other hand, the EOS from high density down to $5\rho_0$ can be derived from QCD using, e.g. functional renormalization group techniques, extended to include strangeness. The trend of predictions towards low densities can be compared to chiral EFT predictions, as has been done for nucleonic matter [19], obtaining the EOS from low to high densities.

The upcoming international Facility for Antiproton and Ion Research (FAIR), foreseen to start operation in 2028, will open up an unprecedented range of exotic ion beams and will provide opportunities for nuclear structure studies on the physics presented above. It aims to be a world-leading, powerful facility for reaching high-intensity radioactive beams produced at energy of up to about 2 GeV/nucleon. The scientific programme at FAIR is divided into the following four pillars: atomic physics, plasma physics and applications; nuclear-matter physics (within the compressed baryonic matter (CBM) and high-acceptance di-electron spectrometer (HADES) experiments); physics with high-energy antiprotons; and nuclear structure, astrophysics and reactions (NuSTAR).

The present Gesellschaft für Schwerionenforschung (GSI) facility already provides relativistic rare-isotope beams produced from primary beams of all stable and long-lived isotopes from ^{1}H up to ^{238}U, which can be accelerated to energies of 4.5 and 1 GeV/nucleon, respectively. The acceleration scheme of the stable primary beams is performed through a three-step chain: ion-source terminals provide charged stable ions, which are then injected into a linear accelerator and transferred into the SIS18 synchrotron [20], where they can be further accelerated up to magnetic rigidity of 18 Tm. The primary beams are transported into the FRagment Separator (FRS) [21] where secondary exotic beams can be produced via in-flight projectile fragmentation or fission. The reaction products are then separated and selected in the FRS through a multistage spectrometer consisting of dipoles and quadrupoles and delivered into the experimental hall.

At FAIR, the existing GSI facility will provide the injector from SIS18 into the new SIS100 (100 Tm) synchrotron [22]. A major gain of 3–4 orders of magnitude is expected in the intensity of the secondary beams compared to GSI [23]. This increase will be feasible via the following twofold development: (i) an increase of 2–3 orders of magnitude in the primary beam intensities by faster cycling and acceleration of lower charge states in SIS18, reducing the space-charge limit and therefore allowing more ions per bunch, and (ii) larger angular and momentum acceptance of the FRS, using the Super-FRS (20 Tm) [24,25]. This is achieved by substantially larger apertures of all ion-optical stages of the separator [26] compared to the FRS.

The Super-FRS will provide the secondary beams for the NuSTAR experiments grouped into low- and high-energy branches. The low-energy branch includes experiments that use ion beams at lower energy than those produced by the Super-FRS. The energy range can be divided into the following different regions: stopped beams, beams with energies at the range of 30–150 MeV/nucleon and stopped and re-accelerated beams (0–60 keV). The directly stopped beams will be used in the DESPEC experiment [27], which focuses on decay spectroscopy of very exotic isotopes. The energetic beams will be used at the HISPEC set-up [27], which aims at in-beam gamma spectroscopy with the highest resolution. The new advanced gamma tracking array AGATA, which will be the core of the HISPEC experiment, is a large-acceptance spectrometer that will have 4π coverage when completed, designed for γ-ray measurements from a few 10 keV to above 10 MeV with high efficiency and excellent resolution [28]. The high-energy branch will include the reactions with relativistic radioactive beams (R^{3}B) set-up, where reactions with relativistic ion beams at the energy range of about 0.3–2 GeV/nucleon will be studied. The physics programme of FAIR has already begun at GSI in 2018 as the FAIR

Phase-0 stage. NuSTAR detectors have been used in experiments, both for their commissioning as well as physics measurements, before final installation at the FAIR site.

In this review, we focus on the physics at the R^{3}B set-up at FAIR. Section 2 presents an overview of the set-up, along with various physics cases in §3 that can be studied and are of high interest for nuclear structure. In addition, further opportunities at FAIR are discussed in §4, including scattering of light ions and electrons in storage rings as well as the concept of multi-GeV experiments with radioactive beams.

2. The R^{3}B experimental set-up

The set-up for the R^{3}B is specifically designed for experiments involving radioactive ions with energies of several hundreds of MeV per nucleon. R^{3}B can accommodate a variety of secondary beams produced at the FRS. This allows experimenting on short-lived relativistic nuclei with significant excess of protons or neutrons, in some cases approaching the drip line limits of nucleon binding.

The secondary beams are delivered to the experimental area of R^{3}B, where event-by-event identification and tracking of individual isotopes are performed by dedicated beam-line detectors. A scintillator-based timing counter provides the time-of-flight (ToF) information with respect to the start detector at FRS, as well as relative to the downstream ToF detectors situated behind the GLAD spectrometer. The ToF is then used for incoming beam identification by extracting its mass-to-charge ratio. The identification is completed with a multi-sampling ionization chamber (MUSIC) [29], where the deposited energy is used to deduce the atomic charge number of the projectile. With the help of tracking detectors based on multi-wire proportional chambers [30], the position and angle of the incoming beams can be accurately measured. The set-up is operating a sophisticated data-acquisition system of multi-channel coincidences and synchronized triggers spread in space over 15 m (equivalent to ToF ≤ 52 ns for massive particles). Figure 1 shows a schematic overview of the R^{3}B experimental set-up. The particular configuration and use of detectors are flexible and can be optimized for each specific experiment.

The reaction target for secondary beams at R^{3}B is chosen according to individual physics cases. In the QFS configuration, a liquid H_2 target is used to induce nucleon or cluster removal from a projectile nucleus. The working principle of the liquid-hydrogen target is as follows (e.g. [35]). The hydrogen is liquefied in a cryostat (cold head mounted on the cryostat and compressor in the vicinity of the cryostat) at a temperature of 19 K. The target relies on the thermosyphon principle, where the hydrogen is both the target material and the cryo-coolant, following the concept of Louchart *et al*. [35]. A vacuum of 10^{-7} mb is imposed in the cryostat and in the target chamber to prevent heat flux via convection. The target cell is made of mylar and composed of an entrance window of 120 µm and an exit window of 180 µm. The target cell diameter is 42 mm, compatible with the beam spot size, and it is further wrapped in several 5 µm thick multi-layer insulation foils to reduce the heat flux via radiation. For this type of experiment, various LH_2 target thicknesses are available with a current maximum of 150 mm. In other measurements, it is possible to use various solid targets of different thicknesses such as, for example, Pb to study Coulomb breakup or pure carbon targets for knockout and other types of reactions.

Owing to the nature of inverse kinematics, the reaction products continue in the forward direction, allowing for an exclusive measurement, where all particles in the final state are detected, leading to a background-free measurement. Owing to relativistic velocities, the reaction products with small transverse momenta are concentrated within a narrow cone around the beam axis and can be guided through the large superconducting spectrometer GLAD [32]—a primary component of the R^{3}B set-up. Its substantial acceptance of ±80 mrad and wide exit aperture with a maximum bending angle of around 40° allow us to measure a variety of forward reaction products, spanning from lightest charged and neutral particles, such

royalsocietypublishing.org/journal/rsta Phil. Trans. R. Soc. A 382: 20230121

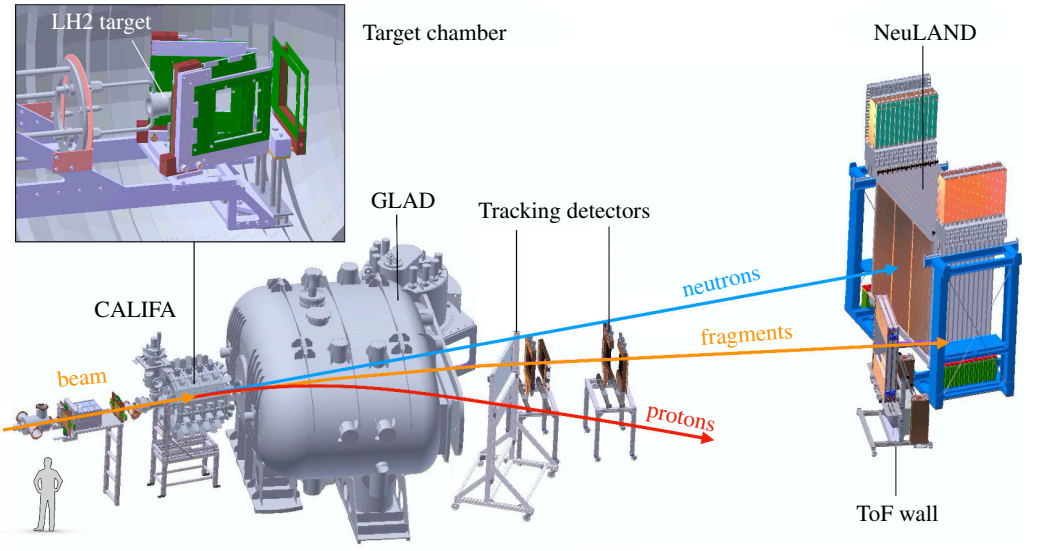

Figure 1. R^{3}B configuration for the first experiment on short-range *NN* correlations in radioactive nuclei [31]. Trajectories of the forward reaction products through the GLAD spectrometer [32] are shown schematically by different colours. Inset figure displays the interior of the CALIFA calorimeter [33,34], which accommodates the LH^2 target chamber together with the target-recoil tracking system. Courtesy of Daniel Körper, GSI.

as protons, neutrons or π-mesons, to heavier ions extending all the way to the trans-lead mass region. A maximum integrated field of 4.8 Tm can be achieved in GLAD, maintaining the field values around 2.2 T in the central region of the spectrometer. Using these settings, a bending angle of 14° at the spectrometer's exit can be obtained for 20 Tm beams.

The large inner gap of GLAD allows, in some cases, placing the reaction targets directly inside the spectrometer, for example, in future experiments dedicated to hypernuclei [36]. In the standard R^{3}B configuration, the target is positioned directly in front of GLAD, inside a vacuum chamber surrounded by the CALIFA calorimeter (CALorimeter for the In-Flight detection of γ-rays and light-charged pArticles) [33,34], as shown in the inset of figure 1. CALIFA serves as a high-resolution spectrometer for γ-rays as well as a calorimeter for high-energy charged particles escaping the reaction target. It is divided into two separate regions: an 'EndCap' for forward polar angles from the beam pipe aperture to 43° and a cylindrical 'Barrel' covering an angular range from 43°to 140°. The Barrel part is composed of 1952 long CsI(Tl) pyramidal frustum crystals [37,38] in six different geometries with a rectangular base, coupled to large area avalanche photodiodes (APDs) with two 10 × 10 mm^2 sensors [39]. The inner radius of the Barrel is around 30 cm, and the Barrel has an approximate crystal volume of 285 l. The forward EndCap is divided into two sections: the inner region, named CEPA, covers polar angles between 7° and 19°, while the outer region, named iPhos, covers polar angles from 19°to 43°. The CEPA and iPhos rings are composed of 112 and 480 CsI(Tl) crystal scintillators, respectively, with a length of around 22 cm similar to the ones in the most forward angles of the Barrel part. These crystals make use of the two scintillation decays in CsI(Tl) to determine the energy deposited by the particles by integrating the signals in a short- and long-time period. The combination of these two variables gives access to the total energy of particles punching through the detector with a resolution of around 13% [40]. The Barrel crystal APDs are read by charge-sensitive pre-amplifier modules. The EndCap APDs are connected to similar pre-amplifiers, which enable the usage of the two gain stages (1×/10× gain) in parallel. The high gain signal is primarily used for low-energy gamma spectroscopy, whereas the low gain signal is mainly used for trigger generation and for the energy measurement of high-energy charged particles, which are either stopped, or punching through the crystals. Gamma-rays emitted by a relativistic nucleus suffer a substantial Lorentz boost so that the energy in the

laboratory frame is strongly correlated with the emission angle. The length of the crystals was chosen to provide the necessary detection efficiency in each angular region. The granularity of the crystals was chosen as a compromise between energy resolution and Doppler broadening. An average angular coverage by an individual crystal is around 3° for polar angles and around 6° for azimuth angles. The resulting energy resolution after the Doppler correction is found to be around 5% for 2.1 MeV γ-ray emitted from ^{11}B moving with a kinetic energy close to 400 MeV/nucleon. Moreover, the kinetic energy of charged particles, such as protons, can be reconstructed with a resolution better than 2% for energies up to 320 MeV.

In addition to CALIFA, a complementary large-acceptance tracking system around the target is essential to reconstruct with high-resolution positions and angles of the outgoing charged reaction products. The required angular resolution provided by such a system should be on the order of a few mrad that corresponds to the missing-mass resolution around a few MeV for $(p, 2p)$ and $(p, 3p)$ reactions at typical R^{3}B energies. Besides that, a reaction vertex in an extended target has to be reconstructed with high accuracy (better than a few mm) to improve the Doppler correction of γ-rays detected by CALIFA. These requirements are fulfilled by the present target-recoil tracking system with two-arm configuration in which each arm consists of an array of four single-sided FOOT-type [41] 150 µm thick and 96 × 96 cm^2 square silicon-strip detectors. The tracking arms are installed in close proximity to the reaction target, as shown in the inset of figure 1. A single FOOT sensor is segmented into 640 readout strips with a pitch size of 150 µm (implant pitch 50 µm) and coupled to the front-end electronics board carrying ten 64-channel charge-sensitive pre-amplifier ASIC chips of a type IDE1140 from IDEAS (Norway). The analogue signals from the chips are digitized by 32-bit ADC units that are coupled to dedicated readout modules based on FPGA boards. The detectors provide high sensitivity to the minimum-ionizing particles and operate with an external trigger signal at the maximum readout rate presently being around 6 kHz. The usage of charge-sensitive pre-amplifiers also allows the use of FOOT as in-beam detectors downstream of the target for tracking and charge identification of outgoing fragments, at least in the case of light-ion secondary beams ($Z < 20$). In the upcoming years, this FOOT-based target-recoil tracker system will be upgraded with a new technology based on ultra-thin silicon-based Monolithic Active Pixel Sensors, called ALPIDE, developed by the ALICE collaboration [42], which were used to equip the ALICE inner tracking device (ITS2). The pixel silicon sensor has a thickness of 50 µm and can provide the position of charged particles with a resolution of around 12 µm full width at half maximum (FWHM) and a detection efficiency above 99%. This new device will allow to increase the readout rate up to 1 MHz and to reconstruct the missing-mass spectra with resolutions of 2–3 MeV (FWHM).

The identification of outgoing reaction fragments passing through the magnetic field of GLAD also requires high-resolution tracking detectors behind the spectrometer. For this purpose, various detectors based on thin scintillating fibres were built. The detectors are produced at GSI where a custom technology is used for winding the fibres and thus arranging them into homogeneous one-dimensional layers. So far a maximum active area of 50×50 cm^2 has been produced. Depending on the experimental needs, different fibre thicknesses of 0.2, 0.5 and 1 mm with square cross-section can be chosen, providing a rather uniform material budget. The scintillating light produced by a charged particle is converted into analogue signals on both ends of a single fibre using either high-density multi-anode PMT (MAPMT) or multi-pixel photon counter (MPPC) from Hamamatsu. The former (MAPMT) is superior in terms of dynamic range, since the gain of the PMT can be easily adopted. On the other hand, using MPPCs allows the detectors to be placed close to the exit of GLAD, where conventional PMTs would suffer from the substantial magnetic fringe field that can reach several tens of mT. Furthermore, the MPPCs allow for a more compact construction of the detector. The PMT signals are processed by readout electronics based on the KINTEX Logic Module, developed at GSI. It consists of a combination of a PreAmplifier DIscriminator together with an FPGA time-to-digital-converter (TDC), providing digital output for the rising and falling times of the

signals with respect to given threshold values. The MPPCs use a slightly different readout based on the DiRich pre-amplifier together with a FPGA TDC combined on one PCB (GSI development). Both readout alternatives allow us to measure the time over threshold that is correlated to the amplitude of the signal. The fibre detectors can provide high individual efficiency above 92% for the detection of charged particles with $Z > 2$ and can operate at the maximum readout rates of a few tens of kHz. The fragment-tracking arm is completed with the ToF detector ToFD, which is able to measure relativistic heavy ions of all charges with relative energy-loss precision of up to 1% and a time precision of up to 14 ps (Sigma) [43]. The detector consists of four planes of 44 vertical scintillator bars with dimensions of $27 \times 1000 \times 5$ mm^3 and the resulting total active area of 1200×1000 mm^2. Overall, the momentum resolution of about $\delta P/P \approx 10^{-4}$ around the reaction target can be achieved from fragment tracking.

For fission studies, a double MUSIC (twin-MUSIC) [29,44–46] is used to obtain the atomic number of the two fission fragments simultaneously. The twin-MUSIC detector has a central vertical cathode that divides its volume into two active regions (left and right), which are divided into two sections (up and down). Each section is segmented into 16 anodes that provide 16 independent energy-loss and drift-time measurements that are read out in parallel by fast high-resolution time and amplitude digitizers (MDPP-16) provided by mesytec. When a fission fragment passes through a section, the energy deposited in the anodes is added to obtain the fission fragment atomic number with a resolution of $\Delta Z \leq 0.4$ (FWHM), as shown in figure 2, whereas the angles on the X–Z plane are obtained from a linear fit of the 16 drift-time measurements with a resolution better than 1 mrad (FWHM).

The Resistive Plate Chamber (RPC) detector, located behind the GLAD superconducting magnet, has been incorporated into the R^{3}B set-up with the goal of precise momentum measurement of light-charged particles (p, d, α, etc.), based on ToF measurement, emitted in the forward direction. It consists of two multi-gap RPC modules [47], where each one is placed in a gas-tight box connected to gas and high voltage via feed-throughs. Each module has six gas gaps created by seven 1 mm thick float glass electrodes of about 1550 ×1250 mm^2 separated by 0.3 mm nylon monofilaments. The two RPC modules are read out simultaneously by a readout strip plane equipped on one side with 41 copper strips (29 mm in width and 30 mm in pitch) with a length of 1600 mm located in between the two modules. The readout scheme is completed by two ground planes at the top and bottom of the two modules. The full assembly is contained in an aluminium box, providing electromagnetic insulation such that it can be placed close to GLAD. In the first beam time commissioning, the detector demonstrated high performances with detection efficiency above 95% and ToF accuracy better than 235 ps (FWHM) [47].

One of the key features of the R^{3}B set-up, provided by the New Large-Area Neutron Detector (NeuLAND) [48], is its highly efficient detection of neutrons with energies above 100 MeV that result from the interaction of the beam in the target. NeuLAND is placed at 0° behind GLAD at a distance of 15–35 m downstream from the target to measure the neutrons, which move undisturbed in the beam direction, not being affected by the magnetic field. In its final configuration, NeuLAND will consist of 3000 individual organic-scintillator submodules of BC-408 type with dimensions of $5 \times 5 \times 250$ cm^3 arranged in 30 double planes with 100 submodules each. This results in a total active area of 250×250 cm^2 and in 3 m thickness of the active material with a spatial resolution of around $\sigma \approx 1.5$ cm. The operation of such a large scintillating array requires a total of 6000 PMTs and a dedicated readout electronics. For this purpose, a special compact multi-channel readout system called FQT-TAMEX with an FPGA-based TDC [49,50] was developed at GSI. The light readout from each scintillator submodule is realized at its far ends by two PMTs coupled to the FQT-TAMEX system. For single neutrons at 400 MeV, the efficiency exceeds 95%. Assuming a single neutron being emitted by a projectile at 600 MeV/nucleon, the resulting resolution of 100 keV (Sigma) is expected when the kinetic energy of the neutron is 1 MeV in the projectile rest frame. Owing to the high granularity and the time resolution of σ_t <150 ps in conjunction with the calorimetric properties,

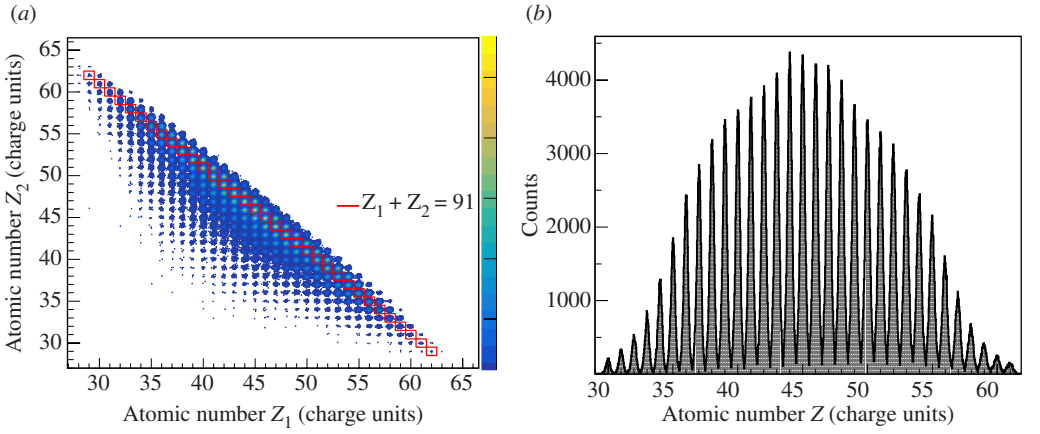

Figure 2. Charge identification (Z) of fission fragments produced in the reaction $^{238}U + p$ at 560 MeV/nucleon. (*a*) Cluster plot showing the correlation between the fission fragment charges. (*b*) Charge distribution of fission fragments for fissioning systems with charge $Z_1 + Z_2 = 91$ produced in single-proton knockout-induced fission reactions. Figures are reprinted from [44,45].

a multi-neutron reconstruction for four-neutron events can be done with the efficiency above 50%. The multi-neutron detection capabilities of NeuLAND will play a key role in future R^{3}B studies, in particular with neutron-rich secondary beams and for nuclear fission experiments.

3. Physics at R^{3}B

(a) Spectroscopy by QFS

Nuclear spectroscopy in inverse kinematics is pivotal to elucidate the properties of nuclei far from stability, where structural changes may occur owing to the drift of single-particle (s.p.) energies, while also impacted by collective degrees of freedom [51,52]. A powerful approach to access the spectroscopy of short-lived nuclei is to deploy direct reactions that involve the addition or removal of one or a few nucleons from a projectile nucleus. As a result, specific particle or hole states can be populated in the final-state system, and the corresponding binding energies, momentum distributions and cross-sections can be extracted. The excitation of the single-hole states through proton-induced QFS reactions such as $(p, 2p)$ and (p, pn) is an established direct method to investigate the s.p. structure and correlations of nuclei. For a comprehensive review of this topic, see [53].

Starting with proton beams in the early 1950s, QFS experiments have provided invaluable insights into valence and deeply bound s.p. orbits in stable nuclei [54–56]. With the advancement of fast RIB, it has become feasible to conduct QFS measurements on unstable nuclei using inverse-kinematics reaction mechanisms and employing hydrogen targets (e.g. [7,57–62]). When complemented by measurements of residual heavy fragments, in-flight gamma spectroscopy and the detection of other reaction products, such as neutrons emitted from unbound final states, these experiments provide an exclusive view of the reaction process.

In the past decade, a series of systematic QFS studies have been conducted across the neutron-rich side of the nuclear chart using RIB with energies around or below 250 MeV/nucleon. Most of the recent prominent results were measured at the RIBF, presently the leading facility to access neutron-rich nuclei. These experiments have employed $(p, 2p)$ and (p, pn) reactions to knockout nucleons, populating ground or low-lying excited states in the residual nucleus, which were identified through coincident γ-rays or neutrons. In the case of even–even light isotopes, the first 2_1^+ state can be interpreted as a single-nucleon excitation between

adjacent s.p. shells. The energy $E(2_1^+)$ associated with this state serves as a measure of the energy gap between the shells. Several robust evidences for the appearance of new magic numbers N= 32 and N= 34 with large $E(2_1^+)$ values have been found via QFS reactions with neutron-rich Ca and Ar isotopes [63–65] as well as from the spectroscopy and mass measurements of the neighbouring isotopes [66–68]. The N= 34 sub-shell closure in ^{54}Ca is notably exemplified by the momentum distribution of the spectator fragment from the ^{54}Ca(p, pn)^{53}Ca reaction and by the corresponding cross-sections to the excited states that unambiguously point to the dominance of p-wave (l = 1) configuration of valence neutrons in the ground state of ^{54}Ca [63]. Further investigations of the Ca isotopic chain above N= 34 have revealed significant deficiencies of the standard theoretical models, which raise doubts about the possible magicity at N= 40 and suggest a shift in the expected neutron drip line for Z= 20 towards N= 50 or beyond owing to predicted degeneracy of $0f_{5/2}$ and $0g_{9/2}$ orbitals [69]. The forthcoming FAIR facility holds promising potential for probing such extreme near-dripline species owing to high intensities and energies of primary beams in GeV/nucleon range.

In the interacting shell-model picture, the s.p. energies are known to be driven by the monopole part of the Hamiltonian. In particular, the roles of the central and tensor terms have been explored in detail, as well as the impact of three-body forces (e.g. [70–72]), on the structure of nuclei far from stability. Besides the formation of large shell gaps and appearance of new magic numbers, these interactions can also induce lowering of the energy separation between s.p. orbitals to the point where intruder configurations become favoured in the ground state. The regions of the nuclear chart where such alterations come into play are known as 'islands of inversion'. As a result, strong quadrupole correlations may occur in even–even nuclei owing to $2p2h$ configurations leading to the onset of collective degrees of freedom and consequently to rapid shape transitions.

Nuclear shapes can be inferred directly by measurements of electromagnetic moments of nuclei. For the case of quadrupole deformation, the spectroscopic quadrupole moment Q_s can be extracted typically via laser spectroscopy from the atomic hyperfine structure [73] or low-energy Coulomb excitation (e.g. [74]). For low-intensity RIB below ~100 particles per second, indirect experimental manifestations of this phenomenon can be captured by low energy E (2_1^+) of first 2^+ states and by an enhanced ratio of E $(4_1^+)/E$ (2_1^+) with respect to the energy of the first 4^+ state reflecting the collectivity of such states [75].

This behaviour was systematically observed in QFS and other knockout reactions populating neutron-rich isotopes ^{66,68,70,72}Fe, ^{64,66}Cr and ^{60,62}Ti around the N = 40 island of inversion [75,76]. The measured E (2_1^+) values in these nuclei are found to be very low, approximately around 500 keV with a flat trend hinting an extended island of inversion towards potential disappearance of the magic number N = 50. At the same time, the doubly magic nature of neutron-rich ^{78}Ni with N = 50 closure and a large E (2_1^+) value at around 2.6 MeV is well-established by QFS reactions ^{79}Cu$(p, 2p)^{78}$Ni and ^{80}Zn$(p, 3p)^{78}$Ni [77]. The observed low-lying second 2^+ state in ^{78}Ni points to a competition between spherical and deformed configurations and to a potential breakdown of Z = 28 shell closure in heavier isotopes with possibly deformed ground states. Future experiments in this region using QFS reactions as a clean and efficient mechanism for populating the low-lying excited states present a compelling avenue for the R^{3}B research programme at FAIR. Complementary measurements of direct two-nucleon removal, e.g. by means of $(p, 3p)$ reaction, were recently suggested as a spectroscopic tool for neutron-rich nuclei. $(p, 3p)$ cross-sections have been measured for various heavy nuclei ($A \gtrsim 70$) [78], where its kinematics was found to be consistent with two sequential p–p collisions in the projectile.

The spectroscopic information for heavier nuclei in the vicinity of the neutron drip line is also a highly demanded input for modelling the r-process nucleosynthesis. In the absence of experimental data in this region, the r-process network calculations have to rely on various approximations and theoretical models for nuclear masses, β-decay half-lives and

neutron-capture rates. A particular source of discrepancies arises from the neutron separation energies calculated with different mass models. Owing to the weakly bound nature of the neutron-rich nuclei, the separation energies have to be known to a good accuracy as it significantly impacts the nucleosynthesis path and resulting chemical abundances [79]. In this respect, nuclear deformations play an important role owing to rapid changes of the separation energies and β-decay half-lives in the regions where the deformations in the ground state or shell closures are present [80]. Theoretically, at least two regions of deformations have been suggested for $30 < Z < 92$, namely $90 < A < 110$ and $130 < A < 170$, both at the mass regions that will be accessible at FAIR. The ions in this mass region can be observed in a fully stripped state, which allows an unambiguous identification. At lower beam energies, the presence of various charge states for the same ions complicates the determination of the nuclear A and Z numbers, necessitating higher experimental resolutions. This mass region will be studied at FAIR via mass measurements at the storage rings, as well as the high-resolution programmes at HISPEC/DISPEC experiments. Direct reactions with high-energy relativistic beams at R^{3}B will also contribute.

Another source of uncertainties in r-process calculations can follow from the evaluation of neutron-capture reaction rates when they are extracted from the statistical Hauser–Feshbach model. This approximation is applicable when the level density in a compound system is sufficiently large, which may not always be the case for weakly bound systems where the neutron capture populates near-threshold states, and hence the role of individual unknown resonances (as well as the direct-capture process) can be important for the reaction rates [81]. As described above, the γ-spectroscopy with QFS reactions provides a suitable approach to gain first knowledge on the excitation energies, nuclear shapes and deformations in regions only accessible with RIBs of intensities less than ~100 particles per second.

The high neutron detection capabilities of the R^{3}B set-up provide additional means of spectroscopy for weakly bound neutron-rich systems using QFS reactions or Coulomb dissociation, which can also be instrumental to advance the r-process studies. The lower separation energies of neutron-rich nuclei lead to a large fraction of the population of unbound states. These can be probed typically using one of two approaches. The missing-mass method, where the energy of the unbound state is not measured directly but reconstructed via, e.g. the kinematics of the scattered protons in the $(p, 2p)$ reaction. Or the invariant-mass measurement, where the energy spectrum is reconstructed via the decay particles including the emission of neutrons.

(b) Multi-neutron systems and halos

The weak binding of valence neutrons at the region of the neutron drip line leads to the occurrence of unusual phenomena such as halo nuclei and clusters of few neutrons. Understanding the interaction of neutrons in such extreme conditions of very large isospin asymmetry and low-density environment is fundamental. At low densities, the *nn* interaction is dominated by the *s*-wave interaction, which is very attractive and, although cannot bind two neutrons into a bound di-neutron state, leads to a well-known virtual state, unbound only by about 100 keV (e.g [82]). This makes the absolute value of the *nns*-wave scattering length very large, $a_{nn} = -18.9(4)$ fm [83]. Therefore, even at very low densities, where the average distance between two neutrons is much larger than the effective range of the interaction, there are still strong correlations. Multi-neutron systems, as pure neutron systems, can provide an exclusive way to address neutron correlations and nuclear structure at the limit of nuclear stability in the absence of the Coulomb interaction. Owing to their high-impact potential, the question whether such nuclear systems can exist led to extensive studies.

In free space, the di-neutron does not exist as a bound state or as a resonance. Yet, di-neutron correlations were found in two-neutron halo nuclei like ^{11}Li as a prime example. The correlation

can be explored by considering the average opening angle between the two halo neutrons. In the absence of a correlation, it equals 90° and increases as the di-neutron correlation becomes stronger [84]. The latest result was obtained via a quasi-free (p, pn) knockout reaction where the di-neutron correlation was investigated as a function of the intrinsic momentum of the knocked-out neutron and was found to be localized on the ^{11}Li surface [85]. More recently, this study was extended to ^{14}Be and ^{17}B [6], where periphery di-neutron correlation was observed, although less pronounced, indicating its universality.

Experiments searching for heavier multi-neutron systems have started already in the early 60s (see [86] for a review), using fission, pion-induced double-charge-exchange (DCX) and transfer reactions. None of those attempts resulted, however, in any indication for multi-neutron existence. Such experiments face the following two main challenges: how to produce multi-neutron systems and how to detect them. In general, the neutron detection efficiency is much smaller compared to charged particles, and it drops exponentially for several neutrons. In practice, it is further reduced when reconstructing the neutrons in a detector owing to cross-talk effects, i.e. when one neutron interacts in the detector several times and can be misidentified as more than one neutron. To minimize this contribution, it is common to apply rejection algorithms that provide a cleaner measurement but, on the other hand, decrease significantly the detection efficiency. Therefore, in most experiments performed so far, the neutrons were not detected and, instead, other methods such as the missing mass have been used. Only very recently, the first measurement of four neutrons in coincidence was demonstrated at the RIBF, which led to the observation of the low-lying ^{28}O resonance [87]. In this experiment, ^{28}O was reconstructed from its decay into ^{24}O + 4n, in a set-up that included also the NeuLAND demonstrator (four double planes) from R^{3}B, with an overall 4n detection efficiency of 0.4% at a decay energy of 0.5 MeV.

With the development of RIB facilities worldwide, it became feasible to use exotic beams, where if multi-neutron systems exist, one would expect an enhanced formation in such a neutron-rich environment. Indeed, the first positive signal appeared in 2002 [88] using a breakup reaction ^{14}Be→^{10}Be + 4n, where six candidate events were suggested to attribute from a bound tetra-neutron or a low-energy resonance ($E_r \leq 2$ MeV) [89]. In 2016, a candidate 4n resonance was observed using the ^{8}He (^{4}He, ^{8}Be) DCX reaction [90]. By measuring four events that were shown to be inconsistent with the continuum response, a possible correlated 4n state was suggested, with energy and width of $E_r = 0.8 \pm 1.4$ MeV and $\Gamma \leq 2.6$ MeV.

These indications motivated many theoretical investigations. A common conclusion is that a bound 4n does not exist. However, model predictions for a resonant state are partly contradictory. Some predict a low-energy resonance using an approach in which the 4n system is artificially bound in an external potential well and then extrapolates to the continuum at vanishing potential strength (e.g. [91]). Others use the no-core shell-model approach extended to the continuum (e.g. [92]) while solving the many-body problem. On the other hand, calculations that treat the continuum directly do not find any 4n resonance in a physical region (e.g. [93,94]).

Recently, an unambiguous 4n correlation has been observed via quasifree ^{8}He(p, $p\alpha$) knockout reaction at RIBF [95]. In the 4n missing-mass energy spectrum, a low-energy peak with a resonance-like structure was observed at an energy of $E_r = 2.37 \pm 0.58$ MeV and a width of $\Gamma = 1.75 \pm 0.37$ MeV. Its interpretation is still under discussion. Triggered by the result, a first calculation constructed a reaction model that is based on a transition between the (α + 4n) initial state and four interacting neutrons in the final state [96]. It suggests that the low-energy structure is induced by the nn final-state interaction (FSI), i.e. two-di-neutron correlations as well as the presence of di-neutron clusters in the initial ^{8}He state.

It should be noted that an indication for a bound 4n state was reported recently using a multi-nucleon transfer reaction ^{7}Li (^{7}Li, ^{10}C) [97], although with relatively low significance.

Quasifree knockout reactions such as $(p, 2p)$, (p, pn), $(p, p\alpha)$ or $(p, 3p)$ are an efficient tool to populate multi-neutron systems. In order to further understand the structure of the observed tetra-neutron correlation and its origin, the next essential step is to perform experiments detecting directly the correlations among the neutrons, by measuring all four neutrons in coincidence. For example, such an experiment is planned at the RIBF using $(p, p\alpha)$ and $(p, 3p)$ reactions.

The NeuLAND array at R^{3}B will be the most suitable for these studies as it will provide a substantial increase in the detection efficiency for multi-neutrons compared to existing neutron detectors worldwide, with estimated reconstruction efficiency around 50% for four neutrons, and an excellent energy resolution of ~30 keV (σ) at relative energy around 100 keV [48]. This will also allow us to take the research field to the next level and go beyond the 4n system searching for hexa-neutron correlations by detecting six neutrons in coincidence, not feasible at present.

Another aspect is to study multi-neutron correlations in neutron-rich nuclei at the region of the drip line, where multiple di-neutron clusters may appear. The start-up version of NeuLAND has been used during the FAIR Phase-0 programme of R^{3}B. Already with the current configuration of 13 double planes, the 4n detection efficiency will be improved by an order of magnitude compared to recent measurements discussed above. In spring 2022, an experiment took place at R^{3}B with the aim to investigate multi-neutron correlations close to and at drip line nuclei [98]. $(p, 2p)$ and (p, pn) reactions were employed to study two- and four-neutron emission from exotic nuclei such as ^{20}C, ^{17}B, ^{14}Be, ^{14}B and ^{11}Li, which will allow us to search for possible di-neutron configurations. The data are currently under analysis, where already 2n events have been reconstructed successfully with NeuLAND.

The structure of halo nuclei is investigated using various experimental probes and observables resulting from the dynamical changes in such systems compared to stable nuclei. The halo physics was triggered by interaction cross-section measurements of light neutron-rich nuclei from He to Be isotopes [4]. The interaction cross-section σ_I is related to the reaction cross-section σ_R by $\sigma_I = \sigma_R - \sigma_{\rm inel}$, with $\sigma_{\rm inel}$ the inelastic cross-section. In the analysis of σ_R, the inelastic contribution should be determined and removed. Inelastic excitation to unbound states can be followed by evaporation of neutrons, for which forward neutron detection set-up, as possible with the NeuLAND array, is essential. Halos exhibit a much larger matter radius compared to the conventional $A^{1/3}$ dependence. In a simplified approximation, the matter radius can be extracted from the measured interaction cross-section by geometrical means. More realistic relations can be obtained using a microscopic reaction model with density profiles as inputs.

So far, several halos have been discovered, although with a limited number of measured nuclei, in particular at mid-mass region. As the neutron drip line is only established up to neon, a compelling question is whether halos can exist in this region and beyond it. Large-scale mean-field predictions resulted in neutron halos candidates for mid-mass nuclei [99]. Systematic interaction cross-section and reaction cross-section measurements for Ne [100] and Mg [101] isotopes, respectively, revealed an enhancement of the cross-section for the neutron-rich isotopes. In particular, around the drip line, ^{31}Ne and ^{37}Mg exceed significantly the values of neighbouring nuclei, suggesting a p-wave halo structure coming from sd–pf shell inversion.

A direct consequence of the halo structure is an enhanced electric dipole ($E1$) response at low excitation energies, 'soft dipole response' (SDR), predicted already in the late 1980s [5]. For stable nuclei, the $E1$ strength appears mainly in the giant dipole resonance (GDR) at excitation energy $E_x \sim 80/A^{1/3}$ MeV. In halo nuclei, the valence neutron(s) may oscillate against the core leading to a significant $E1$ strength well below the GDR energy at $E_x \sim 1$ MeV. For 1n halos, a non-resonant SDR is found at low excitation energies, e.g. ^{11}Be with a pronounced enhancement observed below 1 MeV [102], directly related to the radial extension of the halo. The position of the peak in the $E1$ strength distribution is sensitive to the separation energy, while the shape and amplitude to the angular momentum and spectroscopic factor [103]. For 2n halos, e.g. ^{6}He

[104] and ^{11}Li [84], the dipole response is also understood as attributed from a non-resonant origin, but correlations between the two neutrons in the initial and final state strongly affect the distribution [103].

The scale separation in halo nuclei can be exploited by EFT. Halo EFT is a modern version of nuclear cluster models that provides a controlled framework to calculate the properties of halo nuclei [105], based on a systematic expansion in the ratio of momentum scales $M_{\text{low}}/M_{\text{high}}$, where the halo nucleons are associated with the low momentum scale M_{low}. It was proven successful in describing the low-energy part of the dipole strength of 1n halos such as ^{11}Be [106]. For 2n halos, the $E1$ response was calculated, e.g. in ^{11}Li [107] including a detailed investigation of FSI, showing good agreement with experimental data [84].

Experimentally Coulomb breakup reactions have been used to study the $E1$ strength of exotic nuclei, i.e. the process of heavy-ion induced electromagnetic excitation, where the particle decay after the excitation is measured. Halo systems typically decay into the core plus the halo neutrons. In an inclusive measurement, an integrated cross-section is extracted, assessing whether SDR occurs or not. An exclusive measurement allows us to extract the energy-differential cross-section and assess the halo s.p. state, i.e. the separation energy, angular momentum and spectroscopic factor. For the mid-mass nuclei ^{31}Ne and ^{37}Mg, large inclusive Coulomb breakup cross-sections have been measured [108,109], which indicate the presence of strong low-lying $E1$ transitions. Comparison with calculations suggests that the results are consistent with a significant p-wave halo component in their ground state. If confirmed, ^{37}Mg will be the heaviest halo observed so far. As the conclusions are very model-dependent, follow-up exclusive measurements are requested.

Next-generation experiments of p-wave halo candidates, as well as an extension to heavier potential halos, will allow us to further investigate the nature of the halo phenomenon and the shell evolution. Alongside, measurements with an increased precision and more complete detailed studies for light nuclei will improve our understanding. The R^{3}B set-up will provide such experimental opportunities for measurements of exotic nuclei in a wider mass range. This also includes measurements of the dipole response of non-halo neutron-rich nuclei, currently very rare, reaching up to tin isotopes.

The density profile can be extracted from proton elastic scattering, a tool to deduce the matter radius of a nucleus from the measurement of the differential cross-section at low momentum transfer covering the first diffraction minimum. Such measurements were performed for example at RCNP (e.g. [110]) in direct kinematics for stable nuclei. The measured centre-of-mass (c.m.) angular distribution can be interpreted within a theoretical reaction framework using an optical potential. An experimental challenge in inverse kinematics is that low momentum transfer (small c.m. scattering angles close to $\theta_{\text{lab}} = 90°$) leads to low-energy recoil protons, which limits the achievable resolution in the determination of their scattering angle and energy (see §4(a)). This can be overcome using an active gas target, a hydrogen-filled ionization chamber, which serves both as a target and as a detector for recoil protons.

The method was applied successfully at GSI using IKAR active target on several light nuclei including He and Li isotopes at energies around 700 MeV/nucleon [111] (see figure 3 with the example of ^{6}He). In this initial measurement, only the very low momentum transfer region was probed owing to the limited coverage of the active target to $\theta_{\text{lab}} \simeq 90°$. It was later extended to higher momentum transfer using a new experimental set-up with a liquid-hydrogen target [112]. As shown in figure 3, these data points reach the region of the first diffractive minimum, which provides higher sensitivity to the density distribution. The analysis of the combined spectrum within the Glauber model allowed us to extract the matter radius of ^{6}He as well as information on its structure in terms of the α-core and di-neutron halo radius.

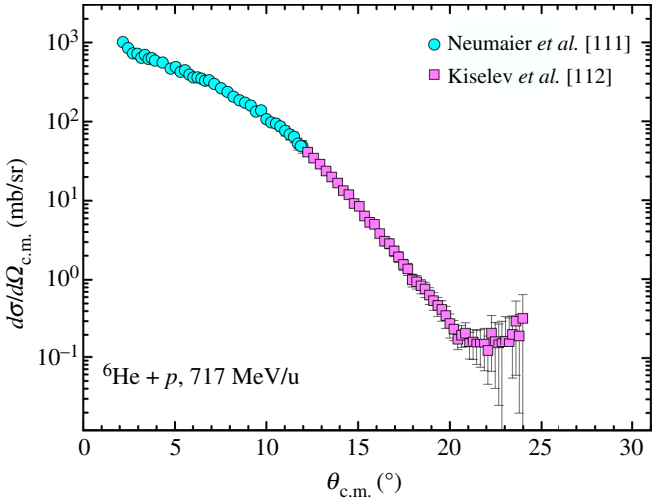

Figure 3. Elastic proton scattering in inverse kinematics off ^{6}He at 717 MeV/nucleon. The circles shown for the low-momentum-transfer region have been taken with the IKAR active target at GSI [111], while the higher momentum transfer measurements (squares) with a liquid-hydrogen target [112]. Figure are reprinted from [113].

(c) Short-range correlations

The mean field, assuming that the ground-state wave function can be described by a Slater determinant, is a first approximation of the nucleus. However, occasionally two nucleons come in close proximity such that they experience the short-range part of the *NN* interaction, which cannot be described by a mean-field approximation. These states are referred to as SRC nucleon pairs, defined in the momentum space as having large relative but small c.m. momentum, with respect to Fermi momentum (k_F~250 MeV/c). Unlike the mean-field approximation, two-body correlations depend directly on the details of the *NN* potential. SRC pairs are formed as temporary fluctuations with high local density, corresponding to several times the nuclear saturation density. These are densities that exist in neutron stars but are difficult to study in the laboratory. Thus, accessing SRCs experimentally in neutron-rich nuclei will teach us not only about the fundamental *NN* interaction but also be used as a possible probe for high densities such as those reached in the core of neutron stars.

Over the last 20 years, electron scattering measurements have been employed successfully to probe SRC pairs and extract their properties. Those were performed mainly at Jefferson Laboratory, using nucleon-knockout reactions at large momentum transfer Q^2>1 (GeV/c^2)^2 (see [114,115] for recent reviews). Experimental signatures of SRC pairs were observed by performing triple-coincidence measurements: detecting the scattered electron in coincidence with the knocked-out nucleon, as well as the correlated partner nucleon that recoils after the breakup of the SRC pair. These experiments demonstrated that at any given moment, about 20% of the nucleons in nuclei ($A \geq 12$) are members of SRC pairs, creating a high-momentum tail in the momentum distribution, absent in the conventional independent-particle model.

The dominant force between SRC nucleons is tensor in nature and acts predominantly on spin−1 isospin−0 neutron–proton (*np*) pairs, leading to a predominance of *np* SRC pairs over proton–proton (*pp*) and *nn* pairs (e.g. [116]). This characteristic was seen experimentally in various nuclei over the nuclear mass range, where *np* pairs were found to be about 20 times more prevalent than *pp* (or *nn*) pairs at the region $300 < p_i < 600$ MeV/c, with p_i the initial momentum of the knocked-out nucleon (e.g. [117–119]). More recently, at higher momenta, a transition from the spin-dependent tensor part to the spin-independent scalar part of the *NN* interaction was proposed after the observation of an increased fraction of *pp* pairs [120].

The isospin asymmetry dependence of SRCs can have consequences for asymmetric nuclei. Measurements with several stable nuclear targets ranging from ^{12}C to ^{208}Pb showed that the fraction of protons forming SRC pairs increases significantly as neutrons are added to the nucleus, while that of the neutrons remains fairly constant [121] (figure 4). This observation implies that protons may carry a larger fraction of momentum than neutrons in neutron-rich nuclei far from stability or in neutron-rich matter. Electron scattering measurements are limited, however, to stable nuclei. As such, the neutron excess dependence shown in figure 4 includes also a mass dependence (^{208}Pb versus ^{12}C). To study the isospin degree of freedom solely, RIB facilities are the only way to do so, where measurements can be performed along isotopic chains, including exotic nuclei.

A unique advantage of experiments in inverse kinematics is the ability to perform a kinematically complete measurement. Unlike direct kinematics, the residual $(A-2)$ system after the SRC pair breakup can be measured in coincidence, allowing us to measure the final state directly. In case of fragmentation of the $(A-2)$ state, it can be reconstructed via its decay products. Moreover, the coincidence of the residue fragment provides an essential suppression of initial-state interaction (ISI) and final-state interactions (FSI) and a cleaner selection of single-step processes.

A pioneering experiment was performed at inverse kinematics using a stable ^{12}C beam at an energy of about 3 GeV/nucleon at JINR [122] using quasifree $(p,2p)$ reaction. First, the single-proton knockout channel was analysed, and it was demonstrated that indeed ISI/FSI are strongly suppressed by tagging in coincidence the residual $(A-1)$ fragment. In a second step, the SRC signal was observed from the coincidence with the $(A-2)$ system, i.e. ^{12}C$(p,2pX)$ with X = ^{10}B, ^{10}Be (the recoil correlated partner was not measured). The results benchmarked the feasibility to access SRC in inverse kinematics with hadronic probes.

Electron scattering experiments show that high-energy beams of at least 1 GeV/nucleon, i.e. momentum transfer of 0.5 $(\mathrm{GeV}/c^2)^2$, and preferably several GeV/nucleon are required in order to resolve SRC pairs. It should be noted, however, that the kinematical limits are not yet established in detail for hadronic probes. In particular, the exclusive nature of inverse kinematics measurements provides additional information that allows resolving states that are challenging to observe in direct kinematics.

The R^{3}B set-up is well suited to perform SRC measurements from RIB at the energy of ~1 GeV/nucleon. With a liquid-hydrogen target, tracking systems for light-charged particles and heavy ions, as well as neutron detection, the set-up comprises all components to perform high-resolution fully exclusive SRC measurements. A pilot experiment was conducted in spring 2022 as part of the FAIR Phase-0 stage, using ^{16}C beam as well as the symmetric ^{12}C as a reference, at the energy of 1.25 GeV/nucleon [31]. A dedicated set-up was designed to perform the first kinematically complete measurement, including not only the $(A-2)$ residue but also the recoil nucleon in coincidence, either a neutron or a proton (figure 1). The data are currently under analysis. The measurement will allow to extract the high momentum fraction of protons and neutrons shown in figure 4, with the advantage of larger neutron-to-proton asymmetry and much smaller mass differences between the two measured nuclei. Successful outcomes will pave the way for systematic studies of the isospin asymmetry along isotopic chains, e.g. the full carbon chain as well as heavier isotopes. As an example, a first physics case has been proposed as part of the Early Science stage at FAIR foreseen in 2028. One interest of inverse kinematics is the possibility to study separately the isospin and mass dependencies. The proposal focuses on ^{132}Sn having similar isospin asymmetry as ^{16}C but very different mass.

Another frontier in SRC physics is the challenging search for three-nucleon ($3N$) SRC. Even though these are expected to occur with a suppressed probability compared to $2N$ SRC, they are essential for our understanding of the NN interactions. So far no conclusive evidence for $3N$ SRC was found from electron scattering experiments, where a few indications have been reported from inclusive (e,e') measurements (e.g. [123]). The increased cross-section for

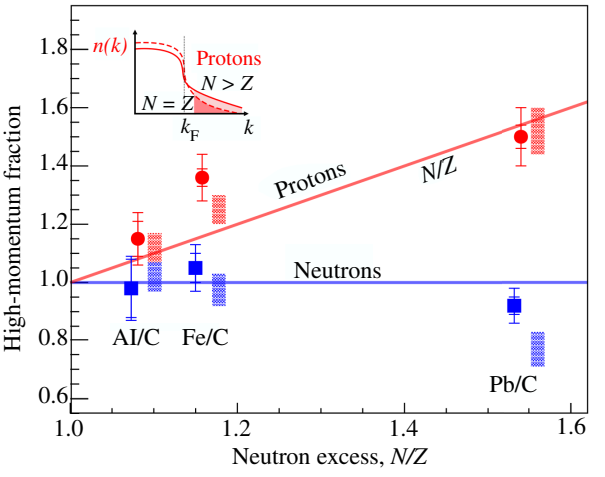

Figure 4. Measured fractions of high- to low-momentum proton (red dots) and neutrons (blue dots) relative to ^{12}C as a function of the neutron excess. Rectangles show the range of predictions based on a phenomenological *np*-dominance model. Figure are reprinted from [121].

hadronic probe compared to the leptonic one and the high-intensity beams provided by FAIR together with the large-acceptance R^3B set-up offer an advantage in search for these triplets.

The long-range plan for SRC studies at FAIR would be the design of an optimized experiment that will allow for both exotic beams and high energies of several GeV/nucleon, which are currently limited to ~1 GeV/nucleon for RIB. This is part of the conceptual multi-GeV experiment described in §4(c).

(d) Nuclear fission

Nuclear fission is the process by which a heavy atomic nucleus divides into two lighter fragments and represents the clearest example of a large-scale collective excitation in nuclei offering a rich laboratory for a broad variety of scientific research on nuclear properties and general physics. Since its discovery in 1939 [124,125], the progress in the understanding of the fission process has been driven by new experimental results. The fission process is a unique tool to investigate the nuclear potential-energy landscape and its evolution as a complex function of excitation energy, elongation, mass asymmetry and spin, passing over the fission barrier (or through it in the case of spontaneous fission) and culminating at the scission point in the formation of fission fragments [126,127]. This transition up to the scission configuration involves a subtle interplay of collective and s.p. effects, such as shell effects and pairing, all of them considered for the initial compound nucleus and for the fission fragments at large deformations. The relatively flat potential energy of fissioning nuclei reaching very large deformations, in comparison to lighter nuclei, allows the investigation of nuclear properties like shell effects in hyper- and super-deformed shapes [128]. Moreover, dynamical phenomena connected with the decay of the quasi-bound nuclear system beyond the saddle point provide information on nuclear transport properties, such as nuclear dissipation [129–133] and heat transfer between the nascent fragments [134].

Fission reactions also play an important role in the r-process itself by fission cycling, for instance, in neutron star mergers where it determines the region of the nuclear chart at which the flow of neutron captures and β-decays stop [135]. Moreover, fission has also been pointed out to produce a robust r-process pattern [136,137], in which the abundances of nuclei with mass number $A \lesssim 140$ are determined during the r-process freeze-out from the fission yields

of nuclei with $A \lesssim 280$ [79]. Recent binary neutron–star merger observations [138,139] confirmed the importance of this scenario for the r-process nucleosynthesis. Here, different fission reaction channels can compete during the r-process nucleosynthesis, but various state-of-the-art simulations have shown that the dominating fission channel contributing to the r-process is the neutron-induced fission one [140], which depends mostly on the fission barrier heights as the process occurs at energies just above the fission barrier. Since no experimental data exist for fission barriers of neutron-rich nuclei involved in the r-process, they have to be modelled [141] to obtain fission reaction rates [142]. In addition, the corresponding fission yields also have to be known for r-process calculations [127,135,143]. The fission yields define the abundance of r-process elements in the second r-process peak and above and can also play an important role in abundance distribution of rare-earth elements [144]. Recently, the importance of forbidden transitions induced by intruder states in the region of $N = 126$ r-process waiting points [145] has been pointed out. These forbidden transitions are predicted to shorten the half-lives of the involved $N = 126$ waiting points significantly and enhance the mass flow through them [79]. As a consequence, the abundances of the second r-process peak around $A = 130$ are affected, and for very neutron-rich ejecta, it is produced mainly by fission yields [79]. The enhanced mass flow also increases delayed α-decays of r-process nuclei that affect the kilonova signals [146]. Therefore, the r-process nucleosynthesis cannot be fully understood without a good knowledge of fission properties of exotic neutron-rich isotopes of the heaviest elements, which cannot be presently accessible via direct measurements.

During the last decades, there has been considerable activity in the field of nuclear fission, both experimental and theoretical. However, despite recent theoretical progress in the investigation of fission, a complete description is still challenging since it is a very complex dynamical process, whose description involves the coupling between intrinsic and collective degrees of freedom, emission of light particles and γ-rays, as well as different quantum-mechanical phenomena [126,147]. Therefore, its investigation requires complex experimental set-ups like R^3B, which allow for complete kinematics measurements of all the fission products.

Since the pioneering experiment carried out at GSI [148] to induce fission reactions of different neutron-deficient actinides and preactinides between the At and U elements, a great effort was made by the Studies On FIssion with Aladin (SOFIA) and R^3B collaborations to overcome the restrictions of conventional fission experiments and to provide complete isotopic measurements of both fission fragments [149,150], inducing fission through spallation, fragmentation and electromagnetic-excitation reactions. An example of the fission-fragment distributions measured in the last two decades at GSI is shown in figure 5 together with other measurements based on particle-induced and spontaneous fission (blue circles) [151–154,156], β-delayed fission (red diamonds) [160,161] and transfer-induced fission reactions (plus symbols) [162–168]. The current R^3B set-up allows us to identify in coincidence both fission fragments in terms of their mass and atomic numbers, as shown in figure 2, with a charge (mass) number resolution better than 0.4 (0.64) units (FWHM) [149,150]. With this approach, it became possible to extract correlations between fission observables sensitive to the dynamics of the fission process [170–173] and the nuclear structure at the scission point [157–159,174]. FAIR will allow us to extend the electromagnetic-induced fission measurements to very neutron-deficient and very neutron-rich fissioning systems to systematically investigate the transitions from asymmetric to symmetric fission regions of each isotopic chain [175]. Moreover, the complete kinematics measurements of fission fragments in combination with the neutron detection provided by the NeuLAND array can allow to study the different reaction channels contributing to the electromagnetic-excitation measurements, in particular, to separate isovector giant dipole and isoscalar giant quadrupole excitations from double giant dipole resonance (DGDR) contributions [176].

The inclusive Coulomb-induced fission mechanism does not allow for the determination of the excitation energy of the fissioning compound nuclei with high precision owing to the width of the DGDR excitation. To go further, those measurements can be combined with quasifree

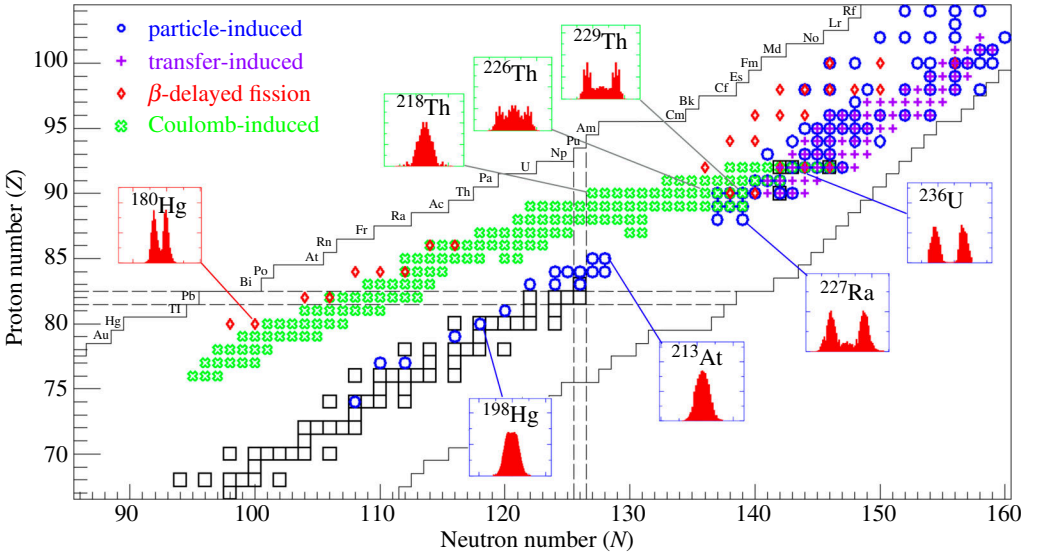

Figure 5. Overview of fissioning systems investigated up to 2023 in low-energy fission with excitation energies up to ~15 MeV above the fission barrier. In addition to the systems where fission-fragment mass distributions were previously obtained in particle-induced and spontaneous fission (blue circles) [151–156], the nuclei for which the fission-fragment charge distributions after electromagnetic excitations were measured in 1996 [148] and in the recent SOFIA/R^{3}B [157–159] experiments in inverse kinematics at GSI are displayed with green crosses. Moreover, fissioning daughter nuclei studied in β-delayed fission (red diamonds) [160,161] as well as around 70 fissioning systems investigated with transfer-induced fission reactions (plus symbols) [162–168] are shown. Several examples of the measured fission-fragment distributions are also displayed to illustrate the transitions. For orientation, the primordial stable isotopes are indicated by black open squares. The limits of known nuclei were obtained from the atomic mass evaluation AME2020 [169].

(p, pn) and (p, $2p$) scattering reactions, which have been proposed as a surrogate mechanism to induce fission of heavy nuclei [8,9,44–46,177]. This approach will allow for reconstructing the excitation energy of the fissioning compound system by measuring the four-momenta of the two outgoing nucleons. In this case, fission is induced by the particle-hole excitations left by the removed nucleon, whose excitation energy ranges from a few to ten's of MeV. Taking into account that fission-fragment yields are characterized by several components in the mass distributions from different fission channels that are attributed to shell effects in the potential energy and by an odd–even staggering in the proton and neutron numbers owing to the influence of pairing correlations, the measurement of the excitation energy in correlation with the atomic and mass number distributions of the two fission fragments represents a powerful tool to investigate the temperature dependence of shell effects [178,179] and pairing correlations [180] for many exotic nuclei. Moreover, this can also be used to study with high accuracy the energy sharing between the nascent fragments [134] by correlating the neutron excess of both fission fragments, as well as to investigate the fission-fragment angular anisotropy evolution with the excitation energy [181,182]. In addition, the excitation energy can be correlated with the fission probability to obtain fission barrier heights, as already performed with transfer reactions of stable nuclei [183,184]. This will also provide unique opportunities to systematically investigate the fission-barrier height dependence on the neutron-to-proton asymmetry [185], helping then to improve the current predictions of astrophysical r-process calculations [135,140,186].

The competition between particle emission and fission decay processes also offers the possibility of studying the repartition of angular momentum between them, governed by the evolution of the nuclear system up to the saddle-point configuration. During the last decades, this partition has been investigated through isomeric states populated by fragmentation

reactions [187–189], and the comparison of experimental data to theoretical calculations based on the abrasion picture [190,191] always resulted in a clear underestimation of the highest experimental angular momentum components by a factor of 10 for heavy nuclei [192,193]. The R^{3}B fission programme has the potential to shed light on the angular momentum gained by the fissioning systems by measuring the fission cross-section as a function of the fissioning system charge, obtained with the sum of fission-fragment charges ($Z_1 + Z_2$). The tail of lighter fissioning systems is mainly populated by abrasion and spallation collisions with very high angular momentum (~100$\hbar$), and the comparison to model calculations would allow us to reconstruct the angular momentum distribution [194]. Therefore, this can give information about the angular momentum carried by the fissioning systems after the abrasion and spallation processes that, complemented with γ-ray multiplicities provided by CALIFA and isomeric states measurements performed by the NuSTAR collaboration [188,189], could provide new data sets to improve theoretical reaction models.

Furthermore, fission reactions can also be used as a tool to investigate non-mesonic decays of heavy hypernuclei (§3(f)). In the 1990s, this approach was used for the first time in the COSY-Jülich facility to measure the lifetime of Λ-hyperons in heavy hypernuclei produced with high energetic protons impinging onto ^{209}Bi and ^{238}U target nuclei. The measurements were performed via the recoil shadow method [195,196] that allowed to obtain the lifetimes and hyper-fission cross-sections for both hypernuclear systems. FAIR may also provide in this case unique opportunities to extend these measurements to exotic nuclei, improving our understanding of the hypernuclei dynamics, in particular the dissipation mechanism in the presence of hyperons [197], and to study systematically the lifetime evolution with the neutron-to-proton asymmetry.

(e) Nuclear EOS

The nuclear EOS underlies the physics of atomic nuclei as well as neutron stars and the synthesis of heavy elements. It is a key ingredient in modelling neutron star formation [198] and, in particular, the gravitational-wave signal from neutron star mergers is sensitive to it [199,200]. Although the size of atomic nuclei differ by many orders of magnitude compared to neutron stars, they are governed by the same EOS. Therefore, observables over the full range of atomic nuclei provide essential input to the EOS. Specifically, measurements of bulk properties of neutron-rich nuclei allow us to put constraints on the EOS.

The EOS of asymmetric matter is often characterized by the symmetry energy $E_{\rm sym}(\rho)$, which represents the variation of the binding energy as the neutron-to-proton ratio in a nuclear system changes. Around ρ_0 it is expanded by its value $J = E_{\rm sym}(\rho_0)$, slope $L = 3\rho_0 \partial E_{\rm sym}(\rho)/\partial\rho|_{\rho_0}$ and the incompressibility $K_{\rm sym} = 9\rho_0^2 \partial^2 E_{\rm sym}(\rho)/\partial\rho^2\big|_{\rho_0}$ at saturation density. Of high importance is the slope parameter L, which despite extensive studies is still poorly constrained experimentally. For example, the slope parameter from analyses of terrestrial experiments is $L = 58.7 \pm 28.1$ MeV and that from neutron star observables $L = 57.7 \pm 19$ MeV [201]. When considering various interaction models that give a good description of ground-state properties of nuclei and their excitations, for the L parameter though, they span over a wide range between almost 0–150 MeV [11]. Its study thus requires a close interplay between experiment and theory. The incompressibility parameter also remains to be determined accurately, where information can be extracted from giant monopole resonances (GMRs) (§4(a)).

An isospin-sensitive observable identified to potentially pin down the L parameter is the neutron-skin thickness $\Delta r_{np} = \sqrt{\langle r_n^2 \rangle} - \sqrt{\langle r_p^2 \rangle}$ of neutron-rich nuclei. About 20 years ago, it was pointed out, using non-relativistic Skyrme Hamiltonian for nuclear Hartree–Fock calculations, that the neutron radius can be related to a new constrain on the neutron EOS [202]. It was then followed by many theoretical studies demonstrating that the neutron-skin thickness is a

very sensitive observable that can be used to determine the slope parameter of the symmetry energy, defined by the neutron EOS. Figure 6*a* shows an example of one of the first calculations, performed for the ^{208}Pb nucleus. The neutron-skin thickness, calculated using different Skyrme Hartree–Fock as well as relativistic mean-field theories, is shown as a function of derivative of the neutron EOS or neutron pressure slightly below saturation density, inherent to the respective interaction used. A clear correlation is observed, suggesting that an accurate measurement of the neutron-skin thickness will provide a precise constraint on the neutron EOS close to saturation density. For exotic nuclei, the effect is more pronounced owing to the development of larger neutron skins [203].

Another isospin-sensitive observable is the dipole polarizability α_D, which reflects influence of an external electric field on the nuclear density. It can be extracted from the isovector $E1$ dipole response of nuclei. An intimate correlation between α_D times J and the neutron-skin thickness was found theoretically [204].

The experimental determination of Δr_{np} is challenging even for stable nuclei, and different techniques have been used over the years. Extraction of the neutron-skin thickness is based on the combination of two measurements. The first is the charge root mean squared (RMS) radius that can be determined precisely by isotopic shift measurements using laser spectroscopy or elastic electron scattering. The second is the matter radius that can be measured for example by proton elastic scattering or via the electroweak interaction in electron scattering. In the case of a hadronic probe, even when precise measurements are performed, model dependencies lead to significant systematical uncertainties. On the other hand, electron scattering is considered to be the cleanest probe and model-independent, but suffers from low statistics. The most accurate Δr_{np} value so far was extracted from the lead radius experiment PREX at the Jefferson Laboratory [205]. Parity-violation asymmetry measurement in elastic scattering of electron from ^{208}Pb at low momentum transfer resulted in $\Delta r_{np} = 0.283 \pm 0.071$ fm, where the main contribution to the uncertainty is the experimental statistics. This result implies a constraint of $L = 106 \pm 37$ MeV [206]. More recently, an asymmetry measurement was carried out for ^{48}Ca in the CREX experiment, resulting in $\Delta r_{np} = 0.121 \pm 0.035$ fm [207], thinner than predicted by models. A combined theoretical analysis of both PREX and CREX found that their asymmetry values are not compatible with the uncertainties [208]. This result still has to be further investigated both from the theory and experiment side. The Mainz Radius Experiment [209] at the MESA electron accelerator at Mainz aims at measuring the neutron skin of ^{208}Pb with higher precision compared to the PREX and CREX measurements. So far electron scattering has been limited to stable nuclei, while an extension to exotic nuclei is ongoing (§4(b)). Proton elastic scattering with RIB can be performed with active target, covering a broad momentum transfer (§3(b)) or in a storage ring (§4(a)).

The dipole polarizability was measured in ^{120}Sn and ^{208}Pb by proton inelastic scattering at angles close to and including 0° at RCNP [210]. It has also been measured in unstable nuclei ^{68}Ni at GSI via Coulomb excitation [12]. A combined analysis resulted in Δr_{np} ranges of 0.15–0.19, 0.12–0.16 and 0.13–0.19 fm for ^{68}Ni, ^{120}Sn and ^{208}Pb, respectively, with a range for the slope parameter $L = 20 - 60$ MeV [211].

A new experimental method to study the evolution of the neutron-skin thickness in neutron-rich nuclei has been initiated at R^{3}B. The basic idea is to measure the total neutron-removal cross-sections $\sigma_{\Delta N}$ in high-energy reactions (0.4–1 GeV/nucleon) of RIB with carbon and hydrogen targets. $\sigma_{\Delta N}$ was shown to be a sensitive observable to Δr_{np} and to the slope parameter L. To demonstrate the feasibility, neutron-rich tin isotopes were investigated for the Sn + ^{12}C reaction. The cross-sections were calculated using density distributions with relativistic mean-field and modified density-dependent (DD2) interaction [212], where the L parameter was changed systematically.

Figure 6*b*(i) shows the relation between the L parameter and $\sigma_{\Delta N}$ for ^{124}Sn and ^{132}Sn, where the relation to the predicted neutron-skin thickness is shown at the bottom. A change of

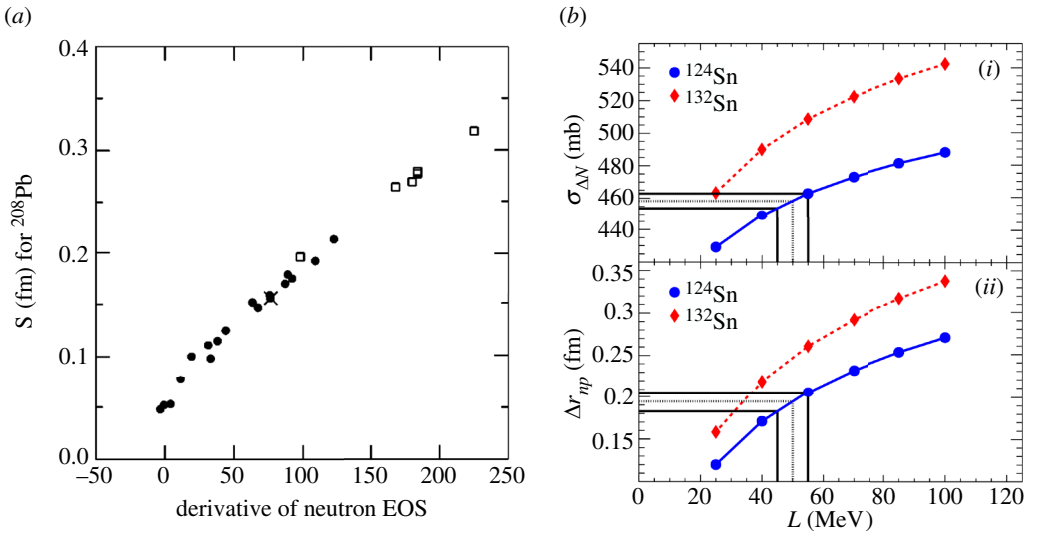

Figure 6. *(a)* Neutron-skin thickness of ^{208}Pb calculated using different Hartree–Fock (filled circles) and relativistic mean-field theories (squares) as a function of the derivative of the neutron EOS at ρ_0 [203]. The cross is the SKX Skyrme Hamiltonian. (*b*) Relation between $\sigma_{\Delta N}$ (i) and Δr_{np} (ii) to the slop parameter L based on relativistic mean-field theory for ^{124}Sn and ^{132}Sn. The black lines indicate the sensitivity to L for a range ±10 MeV. Figure are reprinted from [13].

almost 20% in $\sigma_{\Delta N}$ is visible for ^{132}Sn when the L value ranges from 25 to 100 MeV, while, for comparison, the reaction cross-section σ_R is much less sensitive, with a change of 2.5%. With the interaction used a change of L by ±5 MeV changes $\sigma_{\Delta N}$ by about ±5 mb, i.e. ~1%. Owing to developments of detection techniques, a precise measurement of the neutron-removal cross-section is possible. In addition, variations of the experimental settings such as different targets, energies and ion beams can be used to establish the sensitivity of the method with $\sigma_{\Delta N}$. In particular, to confirm the validity of a parameter-free reaction model and to quantify the associated uncertainties and model dependencies. With that, a possible accuracy of 2% both experimentally and theoretically could be reached, allowing to constrain the slope parameter by ±10 to ±20 MeV, depending on the accuracy of the reaction model. The first set of measurements was taken with beams of $^{124-134}$Sn ions and carbon target at an energy range of 0.4–1 GeV/nucleon [213]. The data from the experiment are currently under analysis.

Once proved successful, this approach will open a new window of opportunities for future experiments to explore the neutron-skin thickness with RIB and study its isospin dependence, as the effect is expected to be more pronounced for increasing neutron-to-proton asymmetry. Complementary to that, theory developments are ongoing, with the goal to reduce systematic uncertainties. In addition, systematic measurements of other observables presented above for exotic nuclei in the tin and lead region, as well as for medium-mass neutron-rich nuclei such as calcium isotopes, would be possible at FAIR and contribute to the efforts for constraining the EOS. In particular, an intriguing result was recently obtained for ^{52}Ca studied via (p, pn) reaction [64]. The measured momentum distributions allowed us to access the RMS radii of the $f_{7/2}$ and $p_{3/2}$ neutron orbitals. The latter was found to be 0.61 ± 23 fm larger, suggesting that the large RMS radius of this orbital in neutron-rich Ca isotopes is responsible for the unexpected increase of the charge radius with the neutron excess. Analysis of momentum distributions after nucleon knockout thus offers a complementary technique sensitive to the RMS radius of s.p. orbitals and should be further exploited to other isotopic chains.

Relativistic heavy-ion collisions give access to matter at extreme conditions of temperature and density and therefore can provide information on the symmetry energy at density higher

than the saturation density. At the present GSI facility, densities up to around $3\rho_0$ can be probed [200]. As the density increases with the incoming beam energy, higher densities can be probed in the future at FAIR.

The following two main observables were identified as sensitive to the EOS [214]: particle multiplicities and ratios, e.g. protons and neutrons, light-charged particles, pions, kaons and their collective flows. The ASY-EOS experiment [215] is planned at R^3B with the goal to measure simultaneously the flow of neutrons and charged particles using Au + Au collisions at energies between 250 and 1000 MeV/nucleon. Its main novelty is the use of the NeuLAND array for measuring neutrons and isotopically resolved H and He isotopes in a broad energy range within the same acceptance. It is a follow-up of a previous measurement performed with the LAND neutron detector [216]. Exploration of the isospin dependence for those observables would be possible with RIB and would provide valuable information to constrain model calculations (§4(c)).

(f) Hypernuclei

Hyperons (Y) are baryons containing at least one strange quark. The Λ is the lightest hyperon, and it decays through the weak interaction with a lifetime of 263 ps [217] into a pion and a nucleon. In the early 50s, it was discovered that hyperons can form bound states with nucleons and create short-lived hypernuclei [218], which decay in the timescale of the weak interaction.

The additional degree of freedom, or strangeness, can result in new symmetries and phenomena that will be revealed by hypernuclei. Studies of hypernuclei are of great importance as they provide a practical way to explore the YN and hyperon–nucleon–nucleon YNN interactions [219]. Since a single hyperon in a nucleus does not suffer from Pauli blocking, it can occupy any orbital inside the nucleus and be used as a probe to the inner densities of nuclei [220]. Adding a hyperon to a nucleus tends to increase the binding energy of the system. Therefore, binding energy data provide information on the YN interaction. The three-body ΛNN interaction that arises from $\Lambda N - \Sigma N$ coupling [221,222] can be investigated by measuring the energies of various hypernuclear levels [220]. Hyperon–hyperon YY interactions can potentially be accessed through double strangeness hypernuclei, although only very few have been synthesized [223].

The YN interactions are also essential for the description of the EOS of dense matter. The expected presence of hyperons at high densities will soften the EOS, resulting in a reduction of the predicted maximum neutron star mass (e.g. [224]), contradicting recent astrophysical observations of a neutron star with two solar masses [225] (the 'hyperon puzzle'). Recent microscopic calculations show that including tuned repulsive ΛNN interactions [226], not constrained at all using current experimental data, could solve this puzzle.

From the theory side, several phenomenological models [227–233] and microscopic shell models [234–239] have been used to describe hypernuclei. Recently, the *ab initio* no-core shell-model framework has been adapted to hypernuclei up into the *p*-shell [240–243] and quantum Monte Carlo methods have been applied to ground-state energies of hypernuclei up into the medium-mass regime [244,245]. While tens of thousands of Λ −hypernuclei are expected to be bound [246], only 41 have been synthesized so far [18], with sometimes debated experimental results, despite decades of experimental efforts. The lack of experimental data affects the current description of the corresponding interactions from a theoretical point of view. New data, in particular on neutron-rich hypernuclei, are essential and would provide benchmark for nuclear theory.

The short lifetime of hypernuclei and the requirement for reactions that involve strangeness impose experimental challenges for hypernuclei studies. In the past decades, meson (K or π) and electron beams have been used to produce hypernuclei at various laboratories such as BNL, KEK and Jefferson Laboratory (see [220] for a review), where a neutron or a proton is converted into a Λ −hyperon, respectively. As stable targets are used in these experiments, they are

limited to near stability. Light hypernuclei are also produced during ultra-relativistic heavy-ion collisions at the cooling stage of the quark-gluon plasma. Extensive measurements have been performed by the ALICE and STAR collaborations, with a focus on the lifetime of hypertriton ${}^{3}_{\Lambda}\mathrm{H}$ (e.g. [247,248]). However, such collisions are only feasible for producing hypernuclei with mass $A \leq (4-5)$, since the production rate drops exponentially with the number of constituents of the cluster [249].

An alternative that has the potential to extend the frame of hypernuclear studies is relativistic ion collisions with projectile energies above the production threshold. In high-energy collisions, the production mechanisms of hyperons are mostly associated with NN collisions, e.g. $p + p \rightarrow p + \Lambda + K^{+}$ (threshold at 1.6 GeV/nucleon) or secondary meson–nucleon collisions, e.g. $\pi^{+} + n \rightarrow \Lambda + K^{+}$ (threshold at 0.8 GeV/nucleon). The produced Λ hyperon can then be absorbed by spectator residual fragments if it overlaps in both spatial and momentum space. Compared to other techniques, since the hypernucleus is created from a projectile fragment, its isospin and mass can be widely distributed. Pioneer experiments with this technique started in the 1970s at Berkeley [250] and continued later in Dubna [251]. The feasibility of the method was further demonstrated recently by the HypHI Phase-0 experiment at GSI using 2 GeV/nucleon ${}^{6}\mathrm{Li}$ projectiles impinging on a carbon target [252]. The known ${}^{3,4}_{\Lambda}\mathrm{H}$ hypernuclei as well as the Λ hyperon were produced and observed successfully following their mesonic decay. As a follow-up of the pioneering experiment, a programme based on the WASA detector at the FRS has been initiated, where the first experiment using the same production reaction was performed in spring 2022 [253]. The future phase of the HypHI project is to extend the measurements towards the drip lines at the Super-FRS at FAIR using a dedicated set-up as a post-WASA detector. This is mostly restricted to neutron-deficient hypernuclei, since from the neutron-rich side, (most) exotic nuclei are not yet accessible owing to the limitation of the magnetic rigidity provided by the FRS (18 Tm) and the Super-FRS (20 Tm). Yet, a new method for producing neutron-rich hypernuclei via single-charge-exchange and DCX reactions with heavy-ion projectiles on a target nucleus, combined with ΛK^{+} production, has been proposed [254].

A new experimental programme has been initiated at $\mathrm{R^3B}$ to study the production of light- and medium-mass hypernuclei from ion–ion collisions. The goal is to perform a complete kinematics measurement of all particles that emerge from the decay of hypernuclei after production from collisions of the ion beam and a fixed target, with high resolution. Light hypernuclei decay mostly via the mesonic decay ($\Lambda \rightarrow \pi^{-} + p$). Considering the two-body channel, the hypernucleus will decay according to a typical lifetime of about 200 ps, to a pion and residual nucleus. A precise measurement of the momenta and identification of the mass and charge for the residual nucleus and decay pion allow us to perform an invariant-mass spectroscopy of the decaying system, i.e. determine its binding energy, lifetime and size. In addition, owing to the large acceptance of the NeuLAND detector at $\mathrm{R^3B}$, other decay channels can also be measured simultaneously.

To achieve the measurement requirements, a dedicated set-up that provides sufficient acceptance and efficiency for pions is necessary. As such, a new pion tracker has been developed, the HYpernuclei Decay at $\mathrm{R^3B}$ Apparatus (HYDRA) time-projection chamber, which will be placed inside the GLAD dipole magnet of the $\mathrm{R^3B}$ set-up. The day-one experiment foreseen in 2025 [255] will be performed with the HYDRA prototype that has recently been built. It aims at determining for the first time the interaction cross-section of the hyperhalo candidate hypertriton ${}^{3}_{\Lambda}\mathrm{H}$ with ${}^{12}\mathrm{C}$. Understood as a universal phenomenon, halos are also predicted in hypernuclei. Hypertriton is the lightest predicted hyperhalo. Although being measured extensively, no measurement of its size has been reported so far. In ${}^{3}_{\Lambda}\mathrm{H}$, the Λ is only bound by 130(50)(40) keV [256] to a deuteron, a reference value from emulsion measurements.

Meanwhile, there is a dispersion of different measurements, which results in different extracted lifetime values, leading to the so-called 'hypertriton puzzle' [257].

In the proposed experiment, projectile-like hypertritons will be produced from ^{12}C + ^{12}C collisions at 1.9 GeV/nucleon and reconstructed via the invariant mass from their weak decay into π^- + ^{3}He. The measurement is a 'hyper' version of the historical Berkeley experiment that led to the discovery of halo nuclei. Based on a new experimental method [36], the interaction cross-section will be determined, allowing extraction of the unknown hypertriton matter radius and providing an unambiguous conclusion on its halo or non-halo character. The extracted matter radius will be key information on the structure of the hypertriton. Its size is believed to be a critical quantity to predict the yield of hypertritons in ultra-relativistic heavy-ion collisions. This experiment will serve as a proof-of-principle to demonstrate the feasibility of hypernuclear invariant-mass spectroscopy, which can then be applied in future experiments at R^{3}B to other hyperhalo candidates such as $^{6}_{\Lambda}$He (S_n = 0.17 MeV) and $^{7}_{\Lambda}$Be (S_{2p} = 0.67 MeV) [258].

Already the $_{\Lambda}$He isotopic chain provides a compelling testing ground for hypernuclear structure theory and *YN* interactions. Recent calculations in the no-core shell model, which fully includes the coupled dynamics of Λ and Σ hyperons, using state-of-the-art chiral *NN* and *NNN* interactions and leading order *YN* interactions. Figure 7 summarizes the excitation spectrum as well as the hyperon separation energies from $^{4}_{\Lambda}$He to $^{10}_{\Lambda}$He and compares them to the experimental data if available. The comparison of the three interactions shows that ground-state, separation and excitation energies show a sensitivity to the *YN* interaction and can be used to better constrain its parameters—this was done using a set of light hypernuclei for the third interaction (YN_{opt}) presented here. Evidently, for large optimizations of *YN*and *YNN* interactions using hypernuclear observables, the availability of accurate data also for neutron-rich hypernuclei will be critical. At present, *ab initio* no-core shell-model calculations are possible up into the $_{\Lambda}$Li isotopic chain [242]. For heavier hypernuclei, development of efficient extensions, such as the in-medium no-core shell model [260], is in progress. This will expand the domain of *ab initio* hypernuclear structure calculations to neutron-rich $_{\Lambda}$C and $_{\Lambda}$O isotopes and beyond.

The long-range plan for hypernuclear studies at FAIR would be an experiment with multi-GeV RIBs that would provide a unique opportunity to study neutron-rich hypernuclei far from stability, unexplored up to date. This is part of the conceptual multi-GeV experiment described in §4(c), where the motivation is detailed below.

The production of single-Λ hypernuclei in relativistic ion collisions was studied using the Dubna cascade model as a function of the projectile energy for ^{12}C + ^{12}C collisions [261]. The yields of hypernuclei increase steeply at the production threshold (1.6 GeV/nucleon), continue to increase linearly up to about 5 GeV/nucleon and flatten out at higher energies. This implies that the optimum to produce single hypernuclei would be in the range of 5–10 GeV/nucleon. The mass distribution of the hypernuclei residues is broad, and the yield of specific hypernuclei depends on the mass and charge of the colliding nuclei. The production of neutron-rich hypernuclei when neutron-rich projectiles are considered may increase significantly, as demonstrated in [262], which extended the calculation for $^{10\text{-}16}$C beams (at 2 GeV/nucleon). Indeed, the results indicate that the production of neutron-rich nuclei increases by two orders of magnitude when the projectile changes from ^{10}C to ^{16}C. Overall, RIB at several GeV/nucleon would enhance strongly the formation of exotic hypernuclei, making their observation feasible.

Of particular interest would be to study the isospin systematics in hypernuclei for mass $A \geq 10$, where the density inside the nucleus reaches the nuclear saturation density. Such new structure information would become a reference to constrain the *YN* and *YNN* interactions. As an example, the systematics of binding energies along isotopic chains of carbon and oxygen would be extended from $^{10}_{\Lambda}$C to $^{19}_{\Lambda}$C and from $^{13}_{\Lambda}$O to $^{21}_{\Lambda}$O, while only very few have been synthesized so far. Such systematics will be sensitive to the isospin dependence of the *YNN*

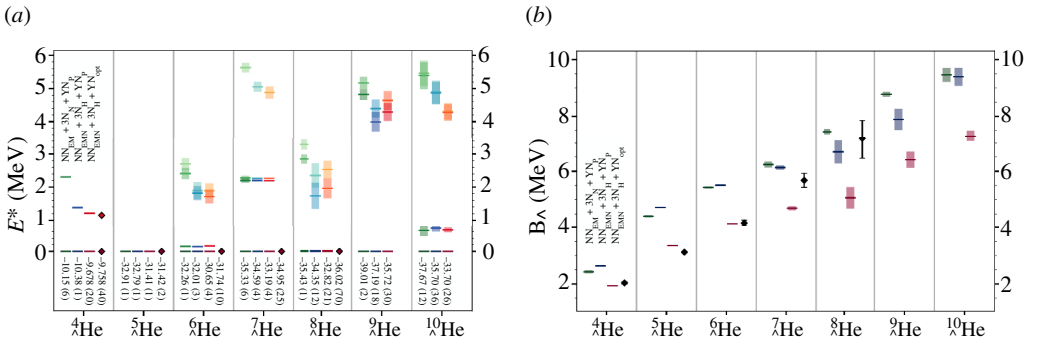

Figure 7. Predictions from the *ab initio* no-core shell model for the ΛHe isotopic chain from $^{4}_{\Lambda}$He to $^{10}_{\Lambda}$He. (*a*) The excitation spectrum with numerical values for the ground-state energies. (*b*) The hyperon separation energies. Three different sets of chiral *NN*, *NNN* and *YN* interactions are employed in the calculations as indicated by the labels. Experimental data are indicated by diamond markers if available. For details, see [259].

interaction since the number of *Ynn* triplets will range from 3 in $^{10}_{\Lambda}$C to 66 in $^{19}_{\Lambda}$C and similarly from 6 in $^{13}_{\Lambda}$O to 66 in $^{21}_{\Lambda}$O.

4. Future developments

(a) Scattering off light ions in a storage ring

Scattering experiments in inverse kinematics focusing on low momentum transfer are particularly challenging. In this case, the light-charged (target) recoils scatter at energies as low as a few hundred keV, which requires in turn very thin targets to allow for precise measurements of the scattering angle and energy. Here, storage rings are advantageous since thin gas-jet targets can be used, while the luminosity loss owing to the thin target is gained back by re-circulation of the stored beam. At GSI, the storage ring ESR, with a frequency of around 1 MHz allows such high-resolution measurements for elastic and inelastic scattering.

A prime example is the excitation of the GMR. The centroid of the GMR strength distribution has been used in the past to extract information on the incompressibility of nuclear matter. It is of great interest to perform such measurements for heavy neutron-rich nuclei to constrain the incompressibility term in the symmetry energy. In order to disentangle the monopole excitation from higher multipoles, the differential cross-section has to be measured as close as possible to 0° in the c.m. frame. Figure 8*a*(i)(ii) shows the angular distribution for different multipolarities for two excitation energies. The data points shown have been measured at the ESR at GSI for ^{58}Ni using a He gas-jet target [263]. Precise cross-sections could be measured at angles as low as 1°, the lowest so far reached in any inverse-kinematics experiment. In this angular c.m. range, the monopole excitation is dominant, allowing for a multipole decomposition without introducing significant model dependencies in the procedure. This experiment, which impressively demonstrated the power of the method, was performed and developed by the EXL collaboration.

The experimental challenge for such experiments is the fact that a storage ring imposes ultra-high vacuum (UHV) conditions. The set-up that has been used is shown in figure 8*b*. Two silicon micro-strip detectors in vacuum pockets have been used to cover the regions of elastic and inelastic scattering, respectively. The detectors serve at the same time as vacuum windows to separate the UHV from the moderate vacuum in the pocket, where the connection to the readout electronics can be placed. The detector covering the angular range important for the

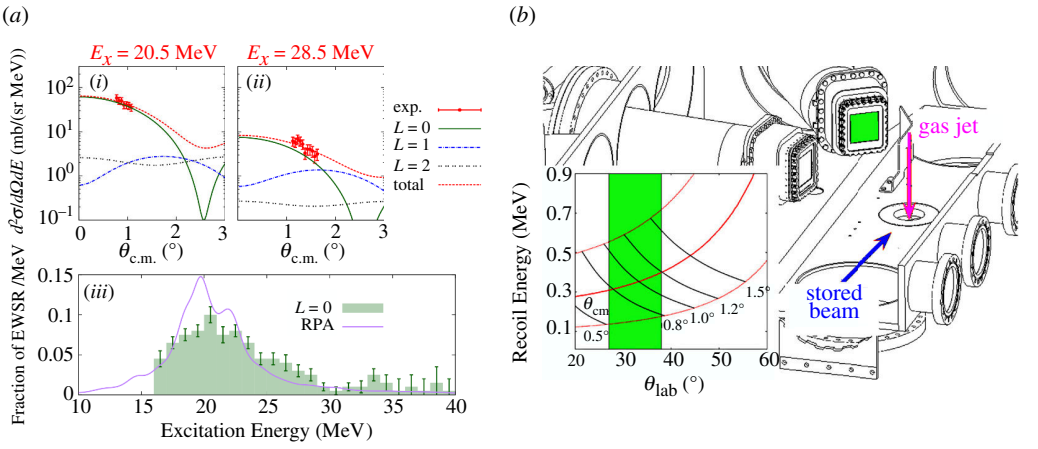

Figure 8. Measurement of the giant monopole strength of ^{58}Ni using inelastic α scattering in inverse kinematics at the storage ring ESR [263]. (*a*(i, ii)) Plots showing the measured inelastic cross-section for two excitation-energy regions together with the decomposition of the cross-sections into monopole, dipole and quadrupole contributions. It is apparent that for scattering angles around 1° in the c.m., the monopole excitation is dominant and can be reliably extracted. The resulting monopole strength is shown below and compared to random phase approximation calculation. (*b*) A schematic drawing of the set-up in the storage ring. The green marked detector has been used for extracting the cross-sections, as also marked in the inset showing the kinematical lines. Figure are reprinted from [263].

monopole excitation is marked in green, as is the angular range covered in the kinematical plot in the inset. The extracted monopole-strength distribution is shown in the figure 8*a*(iii).

The scattering experiments performed so far have been conducted at the ESR storage ring at GSI, either by injecting and cooling direct beams from SIS18 or by using fragment beams from the FRS. The use of radioactive beams is rather limited, given the large emittance of secondary beams and the small acceptance for injection into the ESR. At FAIR, this limitation can be overcome by injecting stochastically pre-cooled Super-FRS beams from the collector ring (CR) into the ESR. This will result in a dramatic improvement in the acceptance of radioactive beams including fission fragments, opening a large area of short-lived nuclei accessible for scattering experiments in the storage ring including key nuclei like ^{52}Ca, ^{68}Ni and ^{132}Sn, as well as ^{208}Pb and beyond. The same injection scheme could be used for electron scattering if an electron accelerator is combined with the storage ring (see below).

(b) Electron-ion collider

Electron scattering measurements exist for many isotopes and are considered as one of the most precise probes for nuclear structure. Currently, however, they are restricted to nuclei in the valley of stability. Collisions of electrons with exotic nuclei are very challenging. The suitable energy of electrons in the c.m. frame should be at the order of several hundred MeV, implying a high-energy electron accelerator at the same place as a RIB facility. In addition, the electron-ion cross-sections are small; thereby, a large luminosity is necessary. Storage rings, on the other hand, have proven to be valuable tools for nuclear structure studies, in particular, when capable of storing RIB.

The combination of a linear electron accelerator with a storage ring can thus enable a systematic study of the development of the charge distribution and radii as a function of isospin asymmetry using elastic electron scattering [264]. Combined with complementary proton elastic scattering measurements, the neutron form factor and the neutron-skin thickness could be determined. Even for relatively low luminosity, a measurement of the differential cross-section

at the low-momentum-transfer range including the first minimum elastic form factor is feasible, giving access to both the radius and shape, i.e. the diffuseness, at the surface of the nucleus.

The concept of using electrons as a probe in conjunction with storage rings filled with RIB was initiated in the early 1990s. The very first facility, which came online in RIKEN, is based on the technique of self-confining radioactive-isotope ion target (SCRIT) in an electron storage ring, where the target ions are trapped along the electron beam axis [265]. As such, it is not a collider properly speaking; the ions are confined by a transverse focusing force created by the electron beam itself and a set of electrodes in a longitudinal direction. At SCRIT, radioactive ions are produced from fission and transmitted at very low energy inside the electron beam. The set-up has been commissioned successfully with stable ^{132}Xe target, reaching luminosity of 10^{27} cm^{-2} s^{-1} [266]. Figure 9 shows the measured elastic differential cross-section distribution multiplied by the luminosity as a function of the effective momentum transfer for different incident electron energies. Assuming a two-parameter Fermi distribution for the charge distribution, its shape parameters were extracted, resulting in RMS radius consistent with theoretical calculations. Very recently, the first measurement of unstable nuclei was performed using ^{137}Cs ions with an average luminosity of 0.9×10^{26} cm^{-2} s^{-1} [267]. The programme of the SCRIT facility focuses on elastic scattering of medium-mass residues. The reachable luminosity will allow the determination of charge radii and the diffuseness. On the other hand, it will not be sufficient to explore the charge distribution of short-lived nuclei [264].

The first proper collider has been proposed at FAIR under electron-ion scattering in a storage ring ELISe facility [268]. The experiments were planned to take place at the new experimental storage ring, which is not part of the upcoming FAIR in its modularized start version (MSV). Therefore, an alternative scheme has been developed: stochastically pre-cooled RIB from the Super-FRS can be extracted from the CR and transported via a beam line at an energy of 740 MeV/nucleon to the existing ESR storage ring at GSI. There, a linear electron accelerator could be installed. The same scheme can be used for in-ring light-ion scattering experiments (§4(a)), where elastic proton scattering can be measured using an internal gas-jet target. Both programmes could be realized already within the MSV, as soon as the CR is available, and will be complementary to each other. The extracted form factor from electron scattering will serve as an input to analyse the proton data, which will then provide the neutron and matter form factors.

Determination of the neutron form factor and neutron radii is fundamental for nuclear structure and benchmark of nuclear theory. Moreover, it is of particular importance for understanding the neutron EOS close to saturation density. As presented in §3(e), a strong correlation is predicted between the neutron-skin thickness and the slope parameter for heavy nuclei close to saturation density, implying that its precise determination will allow us to constrain the symmetry energy of the EOS. For exotic nuclei, the correlation is expected to be more evident, as demonstrated in [203], where the neutron-skin thickness in ^{208}Pb versus that of ^{132}Sn and ^{138}Ba was calculated. While for ^{138}Ba with smaller neutron excess, the predicted skin thickness is smaller, for the doubly magic ^{132}Sn nucleus with a larger neutron excess, it is predicted to be about 30% larger. As a consequence, this also suggests that the slope parameter of the increasing skin thickness as a function of N–Z provides additional constraints on the neutron EOS.

A key measurement in such a facility is therefore the determination of radius, diffuseness and neutron-skin thickness along the tin isotopic chain. The expected luminosities will also allow us to cover a wide range in N–Z ranging from ^{106}Sn to ^{132}Sn. The required luminosity for medium- and heavy-mass nuclei to cover the first minimum and following maximum of the elastic form factor, so that both radius and diffuseness are well determined, lies around 10^{26} cm^{-2} s^{-1}. For ^{132}Sn, the expected luminosity for the scenario described above amounts to 10^{27} cm^{-2} s^{-1}. The trend of development of proton and neutron densities can thus be studied over a wide range of neutron excess from N–Z = 6 to N–Z = 32. In addition, it would also be

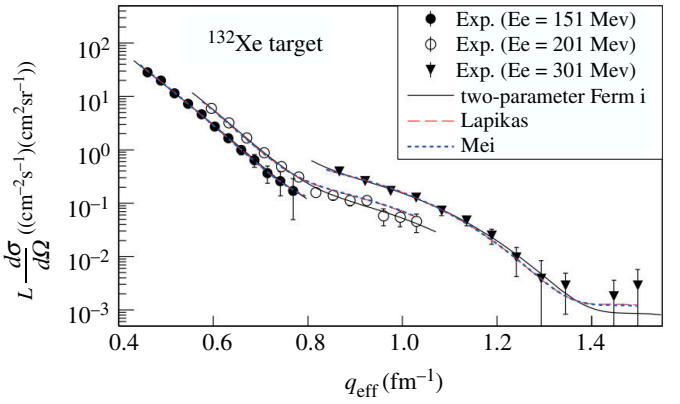

Figure 9. Differential elastic cross-section multiplied by luminosity as a function of the effective momentum transfer for different incident electron energies [266]. The curves represent calculations using a charge density obtained by two-parameter Fermi distribution (black), Hartree–Fock + phenomenological calculation (red) and beyond-relativistic mean-field theory (blue).

possible to perform exploratory quasi-elastic electron scattering studies for light nuclei, as well as electron-induced fission.

(c) Multi-GeV radioactive beam experiments

Despite the development of RIB facilities around the world in recent years, at present, multi-GeV RIBs are not available. As presented in §1, at GSI, the energy of RIB is limited by the maximum magnetic rigidity provided by FRS to 18 Tm, which will increase to 20 Tm for the Super-FRS at FAIR, still not sufficient for producing multi-GeV RIB directly. From a long-term perspective, the concept of re-accelerated RIB produced by the in-flight technique is introduced here, which could be realized at FAIR in a future stage.

Nuclear reactions with RIB at energies of several GeVs at FAIR will lead to world-unique opportunities for new experimental programmes, where in particular physics questions relevant to the physics of neutron stars could be further explored: short-range correlations, hypernuclei, presented in §§3(c) and 3(f), respectively, as well as heavy-ion collisions with large neutron-to-proton asymmetry.

Electron scattering experiments in direct kinematics were not successful in resolving SRCs using beam energies below ~4 GeV, as multi-step processes mask their contribution. This was explained by the lack of a significant difference between the energy scale of SRC and the average energy transfer in the probe–nucleon interaction at moderate energies. Following that, a condition to resolve SRCs was formulated in terms of the energy transfer (ν) and momentum transfer (q_z) [269]

$$\nu \gg k^2/2m_N, \quad q_z \gg 2k, \tag{4.1}$$

with k the intrinsic momentum of the knocked-out nucleon. Although measurements in inverse kinematics provide a much cleaner probe compared to direct kinematics, ideal conditions for an SRC experiment would be RIB at several GeVs, where these scales become quite different and therefore SRCs could be unambiguously measured. As presented in §3(c), the isospin asymmetry dependence of SRCs, observed in stable nuclei, can have consequences for asymmetric nuclei, which can be addressed by the use of RIB.

This energy range will also be extremely beneficial for hypernuclear studies, which are currently mainly limited to hypernuclei close to stability owing to the production threshold at

energy of 1.6 GeV/nucleon. As a consequence of the limited magnetic rigidity and owing to large mass-to-charge ratio of neutron-rich nuclei, only stable or neutron-deficient ion beams can be used. However, as presented in §3(f), the production cross-section of neutron-rich hypernuclei in ion–ion collisions is expected to increase substantially when exotic neutron-rich ion beams are used [262] and is maximal at energy of several GeVs [261]. Therefore, with multi-GeV RIB and a dedicated detection set-up, the landscape of single-Λ hypernuclei can be extended. Information of new hypernuclei, e.g. measured binding energies and lifetimes, will be of particular importance to infer the ΛN and ΛNN interaction for nuclear theory.

Extreme states of baryonic matter, similar to those existing in the interiors of neutron stars or as transient states in merger processes of neutron stars [270,271], can be produced and studied in heavy-ion reactions. This is accomplished by bombarding stationary targets with ion beams at kinetic energies between 1 and 10 GeV/nucleon. Various observables have been identified and used to constrain the EOSs for such baryonic matter under extreme conditions, such as collective motion of protons and light nuclear clusters (flow), the spectral distribution of produced mesons, in particular also kaons carrying strange quarks, higher-order cumulants of baryon multiplicity distribution and recently also the radiation of virtual photons produced during the dense stage of the reactions.

The detection of particles emerging from such reactions requires detectors with large acceptance, high interaction rate, high granularity and excellent particle identification. Heavy-ion experiments using beams from the SIS18 at GSI are limited to energies around 1.25 GeV/nucleon. They were originally carried out by the FOPI and KAOS collaborations and are nowadays performed with the HADES [272–278]. At higher beam energies, the STAR collaboration has investigated heavy-ion reactions, both in collider and fixed-target mode, but with limited rate capability. At FAIR, these measurements will be extended to higher energy regions around 15 GeV/nucleon by the high-rate CBM experiment. As a matter of fact, the isospin composition of the matter investigated in those experiments is dictated by the proton-to-neutron ratio given by the stable nuclei composing the beam and the target.

As already presented in §3(e), angular modulations of the phase-space distribution of emitted particles (flow) have been identified as sensitive observables to the EOS. For example, the so-called elliptic flow of protons, i.e. the second harmonic modulation around the beam axis (v_2), has been suggested to be most sensitive to the EOS [279]. The HADES collaboration has demonstrated that the continuum dilepton radiation can provide a model-independent measure of the average temperature of the transient state of hot and dense matter and also an indirect estimation of the densities reached in the evolving nuclear fireball. Based on studies using microscopic transport models for heavy-ion collisions, it has been conjectured in [280] that pions created in the high-density regions of heavy-ion collisions should, in particular, be sensitive to the symmetry energy term of the EOS.

The SπRIT collaboration has for the first time addressed in detail the isospin dependence of the pion emission by employing unstable beams at the RIBF. The spectral distribution of negatively and positively charged pions has been measured with RIB [281], extending the isospin asymmetry compared to previous studies. Central ^{132}Sn + ^{124}Sn, ^{112}Sn + ^{124}Sn and ^{108}Sn + ^{112}Sn collisions at an energy of 270 MeV/nucleon (maximal at the RIBF) have been investigated, where individual pion multiplicities were extracted with a precision of 4%. Comparing systems with different neutron-to-proton ratios but similar Coulomb effects allows us to study the isospin dependence of the observable. The spectral ratio of charged pions and its sensitivity to the asymmetry term of the EOS have already been studied using microscopic transport models for heavy-ion collisions in [280]. However, the predictive power of microscopic transport calculations suffers when applied to reactions at higher beam energies as the abundant production of baryonic resonances requires many more parameters which are often not well constrained. Moreover, the high density and temperature reached in the centre of the fireball challenge the application of semi-classical transport theory. Yet, simulations of binary neutron star mergers require a prescription of the EOS for densities up to $\simeq 3\rho_0$ and

temperatures in excess of 50 MeV. Such conditions can only be reached in a laboratory for beam energies of a few GeV/nucleon. To better constrain microscopic transport calculations, the models must reproduce several observables simultaneously. It should be pointed out that microscopic transport models are essential for the extraction of the EOS based on data from collision experiments. Various theoretical approaches to study the dynamics of such collisions and to define sensitive observables are pursued [282,283], and a continued effort exists aiming at reducing the model uncertainties [284]. An important aspect is the relevance of the isospin degree of freedom for the EOS once the temperature in the fireball reaches a significant fraction of the pion mass. Under such conditions, charge-exchange reactions are frequent and can lead to a rapid 'equilibration' of the isospin [285]. A huge step forward in constraining the EOS of baryonic matter and the importance of the isospin asymmetry would be achieved by investigating heavy-ion collisions using RIB at a few GeV/nucleon [286] with a state-of-the-art heavy-ion experiment. Such a facility would enable high-statistics measurements of particle emission with the possibility to vary the collision energy and the isospin content of the collision zone.

The concept for the multi-GeV experiments may be based on the use of the CR at FAIR and the post-acceleration of RIB after their production at the Super-FRS. Owing to the large emittance of RIB produced at the Super-FRS, as the first step, they will be transported to the CR. There, fast stochastic cooling will be used to extract low-emittance RIB with momentum spread $\Delta p/p \leq 0.05\%$ and dispersion in the transverse direction better than 0.5 mm mrad [287]. In a second step, the pre-cooled ion beams will be transported via a return beam line at energy of 740 MeV/nucleon and re-injected back into SIS100 for further acceleration up to the desired energy of several GeVs. Finally, beams could be delivered into an experimental area where the reactions of interest will take place, either an existing or new hall that will be equipped with a suitable detector set-up. The cooling and injection stage of RIB from the CR takes about 2 s, which is the main part of the acceleration cycle. This therefore limits the lifetime of the RIB that can be used. Taking this into consideration, possible isotopic chains that can be studied, for example, $^{10\text{-}18}$C, $^{14\text{-}20}$O, $^{40\text{-}48}$Ca, $^{56\text{-}68}$Ni, $^{108\text{-}132}$Sn and $^{187\text{-}215}$Pb, covering a wide neutron-to-proton asymmetry range as well as different mass regions, allowing for systematic isospin studies.

5. Conclusion

The field of radioactive physics has witnessed enormous growth over the past decades, with major advances in understanding exotic nuclei and the properties of nuclear matter. The scientific achievements became possible owing to major upgrades of existing RIB facilities, while new ones are coming online. Yet, this led to some open questions on the structure of medium- and heavy-mass nuclei, the existence of multi-neutron systems, the EOS of neutron-rich matter as well as the role of strangeness in dense nuclear matter.

Since the 1990s, GSI has been a world-leading facility for nuclear structure experiments at the GeV incident energies. The coming soon into operation FAIR facility will provide an increase in RIB intensities by orders of magnitude. As such, it will give access to a broad range of exotic nuclei, reaching unexplored territories of the nuclear landscape. FAIR is unique in terms of its broad energy range of RIB, from a few hundred MeV/nucleon up to relativistic energies above 1 GeV/nucleon, giving access to new regions of excitation energies and unambiguous identification of heavy elements. The physics at FAIR will be of high impact, covering a wide range of many-body structure phenomena as well as astrophysics providing a unique opportunity to address the Universe in the laboratory.

In this review, we focused on the R^3B set-up, which will be installed at the high-energy branch of NuSTAR and is specially designed for experiments involving reactions with RIB, exploiting kinematically complete measurements by detecting all reaction particles in coincidence. The latter will be achieved by several newly developed detection systems, allowing for simultaneous measurement of light-charged particles, gamma-rays, recoil fragments, as

well as neutrons with particular excellent multi-neutron detection capability and high energy resolution.

By using various nuclear reactions and measuring their associated observables, a rich physics outcome is foreseen with new discoveries at and beyond the limit of nuclear stability. Along this review, we presented several highlight cases, with substantial ongoing developments in recent years, that can be addressed uniquely at FAIR with relativistic RIB. In particular, QFS will cover a major fraction through shell evolution and s.p. properties, neutron clusters and fission evolution. Hypernuclear physics is another exciting frontier, giving access to properties of undiscovered hypernuclei and the associated YN interactions, essential for the EOS. Further constrains on the EOS will be determined, for example, by measurements of the neutron-skin thickness along isotopic chains with the highest precision.

New avenues can be realized in the future at FAIR based on the use of storage rings and an electron-ion collider. Finally, the concept of multi-GeV RIB experiments at FAIR is a promising approach to isospin asymmetric high-density nuclear matter.

Data accessibility. This article has no additional data.

Declaration of AI use. We have not used AI-assisted technologies in creating this article.

Authors' contributions. T.A.: writing—original draft, writing—review and editing; C.A.B.: writing—original draft, writing—review and editing; M.D.: writing—original draft, writing—review and editing; T.G.: writing—original draft, writing—review and editing; V.P.: writing—original draft, writing—review and editing; J.L.R.-S.: writing—original draft, writing—review and editing; R.R.: writing—original draft, writing—review and editing; J.S.: writing—original draft, writing—review and editing.

All authors gave final approval for publication and agreed to be held accountable for the work performed therein.

Conflict of interests. We declare we have no competing interests.

Funding. This work was supported by the German Federal Ministry of Education and Research—BMBF project numbers 05P21RDFN2 and 05P21RDFNB, the State of Hesse within the Research Cluster ELEMENTS (project ID 500/10.006), the Deutsche Forschungsgemeinschaft (DFG, German Research Foundation) project ID 279384907—SFB 1245, the GSI-TU Darmstadt cooperation agreement, as well as the Alexandre von Humboldt Foundation.

Acknowledgements. J.L.R.-S. is thankful for the support by the 'Ramón y Cajal' programme under grant no. RYC2021-031989-I, funded by MCIN/AEI/10.13039/501100011033 and by 'European Union NextGenerationEU/PRTR', and by Xunta de Galicia under the programme 'Proyectos de excelencia' grant no. ED431F-2023/43. C.A.B. acknowledges support from the U.S. DOE Grant DE-FG02-08ER41533 and the Helmholtz Research Academy Hesse for FAIR.

References

1. Zhang ZY *et al.* 2019 New isotope ^{220}Np: probing the robustness of the N=126 shell closure in neptunium. *Phys. Rev. Lett.* **122**, 192503. (doi:10.1103/PhysRevLett.122.192503)
2. Ahn DS *et al.* 2019 Location of the neutron dripline at fluorine and neon. *Phys. Rev. Lett.* **123**, 212501. (doi:10.1103/PhysRevLett.123.212501)
3. Sorlin O, Porquet MG. 2008 Nuclear magic numbers: new features far from stability. *Prog. Part. Nucl. Phys.* **61**, 602–673. (doi:10.1016/j.ppnp.2008.05.001)
4. Tanihata I I, Hamagaki H, Hashimoto O, Shida Y, Yoshikawa N, Sugimoto K, Yamakawa O, Kobayashi T, Takahashi N. 1985 Measurements of interaction cross sections and nuclear radii in the light p-shell region. *Phys. Rev. Lett.* **55**, 2676–2679. (doi:10.1103/PhysRevLett.55.2676)
5. Hansen PG, Jonson B. 1987 The neutron halo of extremely neutron-rich nuclei. *Eur. Phys. Lett.* **4**, 409–414. (doi:10.1209/0295-5075/4/4/005)
6. Corsi A *et al.* 2023 Searching for universality of dineutron correlation at the surface of Borromean nuclei. *Phys. Lett. B* **840**, 137875. (doi:10.1016/j.physletb.2023.137875)
7. Panin V, Aumann T, Bertulani CA. 2021 Quasi-free scattering in inverse kinematics as a tool to unveil the structure of nuclei. *Eur. Phys. J. A* **57**, 103. (doi:10.1140/epja/s10050-021-00416-9)

8. Benlliure J, Rodríguez-Sánchez JL. 2017 Spallation-induced fission reactions. *Eur. Phys. J. Plus.* **132**, 120. (doi:10.1140/epjp/i2017-11377-0)
9. Rodríguez-Sánchez JL. 2024 Complete kinematics studies of fission reactions induced by quasi-free nucleon scattering collisions. *EPJ Web Conf.* **292**, 08003. (doi:10.1051/epjconf/202429208003)
10. Schaffner-Bielich J. 2020 *Compact star physics*, p. 147. Cambridge University Press.
11. Roca-Maza X, Paar N. 2018 Nuclear equation of state from ground and collective excited state properties of nuclei. *Prog. Part. Nucl. Phys.* **101**, 96–176. (doi:10.1016/j.ppnp.2018.04.001)
12. Rossi DM *et al.* 2013 Measurement of the dipole polarizability of the unstable neutron-rich nucleus ^{68}Ni. *Phys. Rev. Lett.* **111**, 24503. (doi:10.1103/PhysRevLett.111.242503)
13. Aumann T, Bertulani CA, Schindler F, Typel S. 2017 Peeling off neutron skins from neutron-rich nuclei: constraints on the symmetry energy from neutron-removal cross sections. *Phys. Rev. Lett.* **119**, 262501. (doi:10.1103/PhysRevLett.119.262501)
14. Le Fèvre A, Leifels Y, Reisdorf W, Aichelin J, Hartnack Ch. 2016 Constraining the nuclear matter equation of state around twice saturation density. *Nucl. Phys. A* **945**, 112–133. (doi:10.1016/j.nuclphysa.2015.09.015)
15. Balberg S, Gal A. 1997 An effective equation of state for dense matter with strangeness. *Nucl. Phys. A* **625**, 435–472. (doi:10.1016/S0375-9474(97)81465-0)
16. Baldo M, Burgio GF, Schulze HJ. 1998 Onset of hyperon formation in neutron star matter from Brueckner theory. *Phys. Rev. C* **58**, 3688–3695. (doi:10.1103/PhysRevC.58.3688)
17. Li GQ, Lee CH, Brown GE. 1997 Kaons in dense matter, kaon production in heavy-ion collisions, and kaon condensation in neutron stars. *Nucl. Phys. A* **625**, 372–434. (doi:10.1016/S0375-9474(97)00489-2)
18. Eckert P *et al.* Mainz hypernuclei data base. See http://hypernuclei.kph.uni-mainz.de.
19. Leonhardt M, Pospiech M, Schallmo B, Braun J, Drischler C, Hebeler K, Schwenk A. 2020 Symmetric nuclear matter from the strong interaction. *Phys. Rev. Lett.* **125**, 142502. (doi:10.1103/PhysRevLett.125.142502)
20. Blasche K, Bohne D, Franzke B, Prange H. 1985 The SIS heavy ion synchrotron project. *IEEE Trans. Nucl. Sci.* **32**, 2657–2661. (doi:10.1109/TNS.1985.4334010)
21. Geissel H *et al.* 1992 The GSI projectile fragment separator (FRS): a versatile magnetic system for relativistic heavy ions. *Nucl. Instrum. Methods B* **70**, 286–297. (doi:10.1016/0168-583X(92)95944-M)
22. Guo L, Tian J, Chen P, Derenzo SE, Choong WS. 2020 Improving timing performance of double-ended readout in TOF-PET detectors. *J. Instrum.* **15**, T12013. (doi:10.1088/1748-0221/15/01/p01003)
23. Blumenfeld Y, Nilsson T, Van Duppen P. 2013 Facilities and methods for radioactive ion beam production. *Phys. Scr.* **T152**, 014023. (doi:10.1088/0031-8949/2013/T152/014023)
24. Geissel H *et al.* 2003 The Super-FRS project at GSI. *Nucl. Instrum. Methods B* **204**, 71–85. (doi:10.1016/S0168-583X(02)01893-1)
25. Winkler M *et al.* 2008 The status of the Super-FRS in-flight facility at FAIR. *Nucl. Instrum. Methods B* **266**, 4183–4187. (doi:10.1016/j.nimb.2008.05.073)
26. Winfield JS *et al.* 2021 Ion-optical developments tailored for experiments with the Super-FRS at FAIR. *Nucl. Instrum. Methods B* **491**, 38–51. (doi:10.1016/j.nimb.2021.01.004)
27. Vesić J *et al.* 2023 Simulations of rare-isotope beams for the HISPEC/DESPEC experiments at the Super-FRS. *Nucl. Instrum. Methods A* **1047**, 167714. (doi:10.1016/j.nima.2022.167714)
28. Assari S, Boyce S, Bazargan M, Caldwell CH, Mincy R. 2020 Maternal education at birth and youth breakfast consumption at age 15: Blacks' diminished returns. *J. (Basel).* **3**, 313–323. (doi:10.3390/j3030024)
29. Voss B. 2011 In *Proceedings of the Nuclear Science Symposium and Medical Imaging Conference*.
30. Collaboration A *et al.* 2004 ALICE: physics performance report, volume I. *J. Phys. G: Nucl. Part. Phys.* **30**, 1517–1763. (doi:10.1088/0954-3899/30/11/001)
31. Corsi A *et al.* 2020 First characterization of short-range correlations in exotic nuclei at R^{3}B. G-PAC proposal S522

32. Gastineau B *et al.* 2008 Design status of the R^{3}B-GLAD magnet: large acceptance superconducting dipole with active shielding, graded coils, large forces and indirect cooling by thermosiphon. *IEEE Trans. Appl. Supercond.* **18**, 407–410. (doi:10.1109/TASC.2008.922529)
33. Alvarez-Pol H *et al.* 2014 Performance analysis for the CALIFA Barrel calorimeter of the R^{3}B experiment. *Nucl. Instrum. Methods Phys. Res. Sect. A: Accel., Spectrom., Detect. Assoc. Equip.* **767**, 453–466. (doi:10.1016/j.nima.2014.09.018)
34. Pietras B *et al.* 2016 First testing of the CALIFA barrel demonstrator. *Nucl. Instrum. Methods A* **814**, 56–65. (doi:10.1016/j.nima.2016.01.032)
35. Louchart C *et al.* 2014 The PRESPEC liquid-hydrogen target for in-beam gamma spectroscopy of exotic nuclei at GSI. *Nucl. Instrum. Methods A* **736**, 81–87. (doi:10.1016/j.nima.2013.10.035)
36. Velardita S, Alvarez-Pol H, Aumann T, Ayyad Y, Duer M, Hammer HW, Ji L, Obertelli A, Sun Y. 2023 Method to evidence hypernuclear halos from a two-target interaction cross section measurement. *Eur. Phys. J. A* **59**, 139. (doi:10.1140/epja/s10050-023-01050-3)
37. Knyazev A *et al.* 2020 Tl concentration and its variation in a CsI(Tl) crystal for the CALIFA detector. *Nucl. Instrum. Methods A* **975**, 164197. (doi:10.1016/j.nima.2020.164197)
38. Knyazev A *et al.* 2021 Simulations of light collection in long tapered CsI(Tl) scintillators using real crystal surface data and comparisons to measurement. *Nucl. Instrum. Methods A* **1003**, 165302. (doi:10.1016/j.nima.2021.165302)
39. Cabanelas P *et al.* 2020 Performance recovery of long CsI(Tl) scintillator crystals with APD-based readout. *Nucl. Instrum. Methods A* **965**, 163845. (doi:10.1016/j.nima.2020.163845)
40. Bendel M *et al.* 2015 iPhos, a new technique for the CALIFA CsI(Tl) calorimeter. *J. Phys.: Conf. Ser.* **587**, 012049. (doi:10.1088/1742-6596/587/1/012049)
41. Silvestre G. 2023 Characterization of the microstrip silicon detector for the fragmentation of target experiment. *Nucl. Instrum. Methods A* **1047**, 167717. (doi:10.1016/j.nima.2022.167717)
42. Mager M. 2016 ALPIDE, the monolithic active pixel sensor for the ALICE its upgrade. *Nucl. Instrum. Methods A* **824**, 434–438. (doi:10.1016/j.nima.2015.09.057)
43. Heil M *et al.* 2022 A new time-of-flight detector for the R^{3}B setup. *Eur. Phys. J. A* **58**, 248. (doi:10.1140/epja/s10050-022-00875-8)
44. Graña-Gonzalez A. 2023 Proceedings of FAIR next generation scientists - 7th Edition Workshop. vol. **419**, p. 017,
45. Rodríguez-Sánchez JL *et al.* 2023 Comprehensive investigation of fission yields by using spallation- and (p,2p)- induced fission reactions in inverse kinematics. *EPJ. Web. Conf.* **284**, 04020. (doi:10.1051/epjconf/202328404020)
46. Graña-González A *et al.* 2023 Fission studies in inverse kinematics with the R^{3}B setup. *EPJ Web Conf.* **290**, 02015. (doi:10.1051/epjconf/202329002015)
47. Xarepe M. 2023 Resistive plate chambers for precise measurement of high-momentum protons in short range correlations at R^{3}B. *Nucl. Instrum. Methods A* **1055**, 168445. (doi:10.1016/j.nima.2023.168445)
48. Boretzky K *et al.* 2021 NeuLAND: the high-resolution neutron time-of-flight spectrometer for R^{3}B at FAIR. *Nucl. Instrum. Methods A* **1014**, 165701. (doi:10.1016/j.nima.2021.165701)
49. Ugur C, Bayer E, Kurz N, Traxler M. 2012 A 16 channel high resolution (<11 ps RMS) time-to-digital converter in a field programmable gate array. *J. Inst.* **7**, C02004. (doi:10.1088/1748-0221/7/02/C02004)
50. Ugur C. 2013 *IEEE Nordic-Mediterranean workshop on time-to-Digital Converters*, p. 1.
51. Otsuka T, Gade A, Sorlin O, Suzuki T, Utsuno Y. 2020 Evolution of shell structure in exotic nuclei. *Rev. Mod. Phys.* **92**, 015002. (doi:10.1103/RevModPhys.92.015002)
52. Nowacki F, Obertelli A, Poves A. 2021 The neutron-rich edge of the nuclear landscape: experiment and theory. *Prog. Part. Nucl. Phys.* **120**, 103866. (doi:10.1016/j.ppnp.2021.103866)
53. Aumann T *et al.* 2021 Quenching of single-particle strength from direct reactions with stable and rare-isotope beams. *Prog. Part. Nucl. Phys.* **118**, 103847. (doi:10.1016/j.ppnp.2021.103847)
54. Jacob G, Maris THAJ. 1966 Quasi-free scattering and nuclear structure. *Rev. Mod. Phys.* **38**, 121–142. (doi:10.1103/RevModPhys.38.121)
55. Jacob G, Maris THAJ. 1973 Quasi-Free scattering and nuclear structure. II. *Rev. Mod. Phys.* **45**, 6–21. (doi:10.1103/RevModPhys.45.6)

56. Kitching P *et al.* 1985 Recent developments in quasi-free nucleon-nucleon scattering. *Adv. Nucl. Phys.* **15**, 6. (doi:10.1007/978-1-4613-9898-1)
57. Kobayashi T, Yoshida K, Ozawa A, Tanihata I, Korsheninnikov A, Nikolski E, Nakamura T. 1997 Quasifree nucleon-knockout reactions from neutron-rich nuclei by a proton target: p(6He,pn)5He, p(^{11}Li,pn)^{10}Li, p(^{6}He,2p)^{5}H, and p(^{11}Li,2p)^{10}He. *Nucl. Phys. A* **616**, 223–230. (doi:10.1016/S0375-9474(97)00092-4)
58. Wakasa T, Ogata K, Noro T. 2017 Proton-induced knockout reactions with polarized and unpolarized beams. *Prog. Part. Nucl. Phys.* **96**, 32–87. (doi:10.1016/j.ppnp.2017.06.002)
59. Kobayashi T *et al.* 2008 (p,2p) Reactions on $^{9-16}$C at 250 MeV/A. *Nucl. Phys. A* **805**, 431c–438c. (doi:10.1016/j.nuclphysa.2008.02.282)
60. Pommé S *et al.* 2016 Evidence against solar influence on nuclear decay constants. *Phys. Lett. B* **761**, 281–286. (doi:10.1016/j.physletb.2016.08.038)
61. Aumann T, Bertulani CA, Ryckebusch J. 2013 Quasifree (p,2p) and (p,pn) reactions with unstable nuclei. *Phys. Rev. C* **88**, 064610. (doi:10.1103/PhysRevC.88.064610)
62. Corsi A *et al.* 2019 Structure of ^{13}Be probed via quasi-free scattering. *Phys. Lett. B* **797**, 134843. (doi:10.1016/j.physletb.2019.134843)
63. Chen S. 2019 Quasifree neutron knockout from ^{54}Ca corroborates arising N=34 neutron magic number. *Phys. Rev. Lett.* **123**, 142501. (doi:10.1103/PhysRevLett.123.142501)
64. Enciu M *et al.* 2022 Extended p_{3/2} neutron orbital and the N=32 shell closure in ^{52}Ca. *Phys. Rev. Lett.* **129**, 262501. (doi:10.1103/PhysRevLett.129.262501)
65. Liu HN *et al.* 2019 How robust is the N=34 subshell closure? First spectroscopy of ^{52}Ar. *Phys. Rev. Lett.* **122**, 072502. (doi:10.1103/PhysRevLett.122.072502)
66. Janssens RVF *et al.* 2002 Structure of ^{52,54}Ti and shell closures in neutron-rich nuclei above ^{48}Ca. *Phys. Lett. B* **546**, 55–62. (doi:10.1016/S0370-2693(02)02682-5)
67. Leistenschneider E *et al.* 2018 Dawning of the N=32 shell closure seen through precision mass measurements of neutron-rich titanium isotopes. *Phys. Rev. Lett.* **120**, 062503. (doi:10.1103/PhysRevLett.120.062503)
68. Bürger A. 2005 Relativistic Coulomb excitation of neutron-rich ^{54,56,58}Cr: on the pathway of magicity from N=40 to N=32. *Phys. Lett. B* **622**, 29–34. (doi:10.1016/j.physletb.2005.07.004)
69. Chen S *et al.* 2023 Level structures of ^{56,58}Ca cast doubt on a doubly magic ^{60}Ca. *Phys. Lett. B* **843**, 138025. (doi:10.1016/j.physletb.2023.138025)
70. Neyens G *et al.* 2005 Measurement of the spin and magnetic moment of ^{31}Mg: evidence for a strongly deformed intruder ground state. *Phys. Rev. Lett.* **94**, 232502. (doi:10.1103/PhysRevLett.94.022501)
71. Otsuka T, Suzuki T, Honma M, Utsuno Y, Tsunoda N, Tsukiyama K, Hjorth-Jensen M. 2010 Novel features of nuclear forces and shell evolution in exotic nuclei. *Phys. Rev. Lett.* **104**, 032501. (doi:10.1103/PhysRevLett.104.012501)
72. Lesinski T, Bender M, Bennaceur K, Duguet T, Meyer J. 2007 Tensor part of the Skyrme energy density functional: spherical nuclei. *Phys. Rev. C.* **76**, 014312. (doi:10.1103/PhysRevC.76.014312)
73. Görgen A, Korten W. 2016 Coulomb excitation studies of shape coexistence in atomic nuclei. *J. Phys. G: Nucl. Part. Phys.* **43**, 024002. (doi:10.1088/0954-3899/43/2/024002)
74. Campbell P, Moore ID, Pearson MR. 2016 Laser spectroscopy for nuclear structure physics. *Prog. Part. Nucl. Phys.* **86**, 127–180. (doi:10.1016/j.ppnp.2015.09.003)
75. Santamaria C *et al.* 2015 Extension of the N=40 Island of inversion towards N=50: spectroscopy of (66)Cr, (70,72)Fe. *Phys. Rev. Lett.* **115**, 192501. (doi:10.1103/PhysRevLett.115.192501)
76. Gade A. 2021 Reaching into the N = 40 island of inversion with nucleon removal reactions. *Phys. (Coll. Park. Md.).* **3**, 1226. (doi:10.3390/physics3040077)
77. Taniuchi R *et al.* 2019 ^{78}Ni revealed as a doubly magic stronghold against nuclear deformation. *Nature New Biol.* **569**, 53–58. (doi:10.1038/s41586-019-1155-x)
78. Frotscher A *et al.* 2020 Sequential nature of (p,3p) two-proton knockout from neutron-rich nuclei. *Phys. Rev. Lett.* **125**, 012501. (doi:10.1103/PhysRevLett.125.012501)
79. Mendoza-Temis J de J, Wu MR, Langanke K, Martínez-Pinedo G, Bauswein A, Janka HT. 2015 Nuclear robustness of ther process in neutron-star mergers. *Phys. Rev. C* **92**, 055805. (doi:10.1103/PhysRevC.92.055805)

80. Meshik AP, Pravdivtseva OV, Hohenberg CM. 2016 New evidence for chemical fractionation of radioactive xenon precursors in fission chains. *Phys. Rev. C* **93**, 055802. (doi:10.1103/PhysRevC.93.044614)
81. Rauscher T, Thielemann FK, Kratz KL. 1997 Nuclear level density and the determination of thermonuclear rates for astrophysics. *Phys. Rev. C* **56**, 1613–1625. (doi:10.1103/PhysRevC.56.1613)
82. Hammer HW, König S. 2014 Constraints on a possible dineutron state from pionless EFT. *Phys. Lett. B* **736**, 208–213. (doi:10.1016/j.physletb.2014.07.015)
83. Chen Q. 2008 Measurement of the neutron-neutron scattering length using the π−d capture reaction. *Phys. Rev. C* **77**, 054002. (doi:10.1103/PhysRevC.77.054002)
84. Adler SS *et al.* 2006 J/psi production and nuclear effects for d + Au and p + p collisions at square root of S(NN) = 200 GeV. *Phys. Rev. Lett.* **96**, 252502. (doi:10.1103/PhysRevLett.96.012304)
85. Kubota Y *et al.* 2020 Surface localization of the dineutron in ^{11}Li. *Phys. Rev. Lett.* **125**, 252501. (doi:10.1103/PhysRevLett.125.252501)
86. Marqués FM, Carbonell J. 2021 The quest for light multineutron systems. *Eur. Phys. J. A* **57**, 105. (doi:10.1140/epja/s10050-021-00417-8)
87. Kondo Y *et al.* 2023 First observation of ^{28}O. *Nat. New Biol.* **620**, 965–970. (doi:10.1038/s41586-023-06352-6)
88. Marqués FM *et al.* 2002 Detection of neutron clusters. *Phys. Rev. C* **65**, 044006. (doi:10.1103/PhysRevC.65.044006)
89. Marqués FM *et al.* 2005 On the possible detection of 4n events in the breakup of ^{14}Be (doi:10.48550/arXiv.nucl-ex/0504009)
90. Kisamori K *et al.* 2016 Candidate resonant tetraneutron state populated by the ^{4}He(^{8}He, ^{8}Be) reaction. *Phys. Rev. Lett.* **116**, 052501. (doi:10.1103/PhysRevLett.116.052501)
91. Gandolfi S, Hammer HW, Klos P, Lynn JE, Schwenk A. 2017 Is a trineutron resonance lower in energy than a tetraneutron resonance? *Phys. Rev. Lett.* **118**, 232501. (doi:10.1103/PhysRevLett.118.232501)
92. Shirokov AM, Papadimitriou G, Mazur AI, Mazur IA, Roth R, Vary JP. 2016 Prediction for a four-neutron resonance. *Phys. Rev. Lett.* **117**, 182502. (doi:10.1103/PhysRevLett.117.182502)
93. Meshik AP, Pravdivtseva OV, Hohenberg CM. 2016 New evidence for chemical fractionation of radioactive xenon precursors in fission chains. *Phys. Rev. C* **93**, 044004. (doi:10.1103/PhysRevC.93.044614)
94. Lazauskas R *et al.* 2017 Modeling the double charge exchange response function for a tetraneutron system. *Prog. Theor. Exp. Phys.* **073D03**. (doi:10.1093/ptep/ptx078)
95. Duer M *et al.* 2022 Observation of a correlated free four-neutron system. *Nat. New Biol.* **606**, 678–682. (doi:10.1038/s41586-022-04827-6)
96. Lazauskas R, Hiyama E, Carbonell J. 2023 Low energy structures in nuclear reactions with 4n in the final state. *Phys. Rev. Lett.* **130**, 102501. (doi:10.1103/PhysRevLett.130.102501)
97. Faestermann T, Bergmaier A, Gernhäuser R, Koll D, Mahgoub M. 2022 Indications for a bound tetraneutron. *Phys. Lett. B* **824**, 136799. (doi:10.1016/j.physletb.2021.136799)
98. Sorlin O *et al.* 2020 Study of multi-neutron correlations in drip-line nuclei. G-PAC. prop. S509
99. Rotival V, Bennaceur K, Duguet T. 2009 Halo phenomenon in finite many-fermion systems: atom-positron complexes and large-scale study of atomic nuclei. *Phys. Rev. C* **79**, 054309. (doi:10.1103/PhysRevC.79.054309)
100. Takechi M *et al.* 2012 Interaction cross sections for Ne isotopes towards the island of inversion and halo structures of ^{29}Ne and ^{31}Ne. *Phys. Lett. B* **707**, 357–361. (doi:10.1016/j.physletb.2011.12.028)
101. Takechi M *et al.* 2014 Evidence of halo structure in ^{37}Mg observed via reaction cross sections and intruder orbitals beyond the island of inversion. *Phys. Rev. C* **90**, 061305. (doi:10.1103/PhysRevC.90.061305)
102. Nakamura T *et al.* 1994 Coulomb dissociation of a halo nucleus ^{11}Be at 72A MeV. *Phys. Lett. B* **331**, 296–301. (doi:10.1016/0370-2693(94)91055-3)
103. Aumann T, Nakamura T. 2013 The electric dipole response of exotic nuclei. *Phys. Scr.* **T152**, 014012. (doi:10.1088/0031-8949/2013/T152/014012)

104. Aumann T *et al.* 1999 Continuum excitations in ^{6}He. *Phys. Rev. C* **59**, 1252–1262. (doi:10.1103/PhysRevC.59.1252)
105. Hammer HW, König S, van Kolck U. 2020 Nuclear effective field theory: status and perspectives. *Rev. Mod. Phys.* **92**, 025004. (doi:10.1103/RevModPhys.92.025004)
106. Hammer HW, Phillips DR. 2011 Electric properties of the Beryllium-11 system in Halo EFT. *Nucl. Phys. A* **865**, 17–42. (doi:10.1016/j.nuclphysa.2011.06.028)
107. Göbel M, Acharya B, Hammer HW, Phillips DR. 2023 Final-state interactions and spin structure in E1 breakup of Li11 in halo effective field theory. *Phys. Rev. C* **107**, 014617. (doi:10.1103/PhysRevC.107.014617)
108. Aad G *et al.* 2014 Search for dark matter in events with a hadronically decaying W or Z boson and missing transverse momentum in pp collisions at $\sqrt{s}$=8TeV with the ATLAS detector. *Phys. Rev. Lett.* **112**, 142501. (doi:10.1103/PhysRevLett.112.041802)
109. Nakamura T *et al.* 2014 Deformation-driven p-wave halos at the drip line: 31Ne. *Phys. Rev. Lett.* **112**, 242501. (doi:10.1103/PhysRevLett.112.142501)
110. Terashima S *et al.* 2008 Proton elastic scattering from tin isotopes at 295 MeV and systematic change of neutron density distributions. *Phys. Rev. C* **77**, 024317. (doi:10.1103/PhysRevC.77.024317)
111. Neumaier SR *et al.* 2002 Small-angle proton elastic scattering from the neutron-rich isotopes 6He and 8He, and from 4He, at 0.7GeV in inverse kinematics. *Nucl. Phys. A* **712**, 247–268. (doi:10.1016/S0375-9474(02)01274-5)
112. Kiselev OA *et al.* 2011 A new experimental approach to investigate intermediate-energy proton elastic scattering and breakup reactions on exotic nuclei in inverse kinematics. *Nucl. Instr. Meth. A* **641**, 72–86. (doi:10.1016/j.nima.2011.03.046)
113. Chung LX, Kiselev OA, Khoa DT, Egelhof P. 2015 Elastic proton scattering at intermediate energies as a probe of the ^{6,8}He nuclear matter densities. *Phys. Rev. C* **92**, 034608. (doi:10.1103/PhysRevC.92.034608)
114. Hen O, Miller GA, Piasetzky E, Weinstein LB. 2017 Nucleon-nucleon correlations, short-lived excitations, and the quarks within. *Rev. Mod. Phys.* **89**, 045002. (doi:10.1103/RevModPhys.89.045002)
115. Arrington J, Fomin N, Schmidt A. 2022 Progress in understanding short-range structure in nuclei: an experimental perspective. *Annu. Rev. Nucl. Part. Sci.* **72**, 307–337. (doi:10.1146/annurev-nucl-102020-022253)
116. Wiringa RB, Schiavilla R, Pieper SC, Carlson J. 2014 Nucleon and nucleon-pair momentum distributions in A≤12 nuclei. *Phys. Rev. C* **89**, 024305. (doi:10.1103/PhysRevC.89.024305)
117. Subedi R *et al.* 2008 Probing cold dense nuclear matter. *Science* **320**, 1476–1478. (doi:10.1126/science.1156675)
118. Hen O *et al.* 2014 Nuclear physics. momentum sharing in imbalanced Fermi systems. *Science* **346**, 614–617. (doi:10.1126/science.1256785)
119. Duer M *et al.* 2019 Direct observation of proton-neutron short-range correlation dominance in heavy nuclei. *Phys. Rev. Lett.* **122**, 172502. (doi:10.1103/PhysRevLett.122.172502)
120. Burmann BM *et al.* 2020 Regulation of α-synuclein by chaperones in mammalian cells. *Nat. New Biol.* **577**, 127–132. (doi:10.1038/s41586-019-1808-9)
121. Duer M. 2018 Probing high-momentum protons and neutrons in neutron-rich nuclei. *Nat. New Biol.* **560**, 617–621. (doi:10.1038/s41586-018-0400-z)
122. Patsyuk M *et al.* 2021 Unperturbed inverse kinematics nucleon knockout measurements with a carbon beam. *Nat. Phys.* **17**, 693–699. (doi:10.1038/s41567-021-01193-4)
123. Fomin N *et al.* 2012 New measurements of high-momentum nucleons and short-range structures in nuclei. *Phys. Rev. Lett.* **108**, 092502. (doi:10.1103/PhysRevLett.108.092502)
124. Meitner L, Frisch OR. 1939 Disintegration of uranium by neutrons: a new type of nuclear reaction. *Nat. New Biol.* **143**, 239–240. (doi:10.1038/143239a0)
125. Hahn O, Strassmann F. 1939 Ber den Nachweis und das Verhalten der bei der Bestrahlung des Urans mittels Neutronen entstehenden Erdalkalimetalle. *Nat. Wissensch.* **27**, 11–15. (doi:10.1007/BF01488241)
126. Scamps G. 2018 Impact of pear-shaped fission fragments on mass-asymmetric fission in actinides. *Nat. New Biol.* **564**, 382–385. (doi:10.1038/s41586-018-0780-0)
127. Balantekin AB *et al.* 2020 Nonfuel antineutrino contributions in the high flux isotope reactor. *Phys. Rev. C* **101**, 065803. (doi:10.1103/PhysRevC.101.054605)

128. Delaroche JP, Girod M, Goutte H, Libert J. 2006 Structure properties of even–even actinides at normal and super deformed shapes analysed using the Gogny force. *Nucl. Phys. A* **771**, 103–168. (doi:10.1016/j.nuclphysa.2006.03.004)
129. Fröbrich P, Gontchar II. 1998 Langevin description of fusion, deep-inelastic collisions and heavy-ion-induced fission. *Phys. Rep.* **292**, 131–237. (doi:10.1016/S0370-1573(97)00042-2)
130. Schmitt C, Schmidt KH, Kelić A, Heinz A, Jurado B, Nadtochy PN. 2010 Fragmentation of spherical radioactive heavy nuclei as a novel probe of transient effects in fission. *Phys. Rev. C* **81**, 064602. (doi:10.1103/PhysRevC.81.064602)
131. Mazurek K, Schmitt C, Nadtochy PN. 2015 Description of isotopic fission-fragment distributions within the Langevin approach. *Phys. Rev. C* **91**, 041603. (doi:10.1103/PhysRevC.91.041603)
132. Ayyad Y. 2015 Dissipative effects in spallation-induced fission of Pb 208 at high excitation energies. *Phys. Rev. C.* **91**, 034601. (doi:10.1103/PhysRevC.91.034601)
133. Wang N, Ye W. 2023 Stringent constraints on nuclear dissipation by second-chance survival probability. *Phys. Lett. B* **843**, 138010. (doi:10.1016/j.physletb.2023.138010)
134. Schmidt KH, Jurado B. 2010 Entropy driven excitation energy sorting in superfluid fission dynamics. *Phys. Rev. Lett.* **104**, 212501. (doi:10.1103/PhysRevLett.104.212501)
135. Dulay MT, Zaman N, Jaramillo D, Mody AC, Zare RN. 2018 Pathogen-imprinted organosiloxane polymers as selective biosensors for the detection of targeted *E. coli*. *C. (Basel).* **4**, 29. (doi:10.3390/c4020029)
136. Rosswog S, Korobkin O, Arcones A, Thielemann FK, Piran T. 2014 The long-term evolution of neutron star merger remnants - I. The impact of r-process nucleosynthesis. *Mon. Not. R. Astron. Soc.* **439**, 744–756. (doi:10.1093/mnras/stt2502)
137. Goriely S. 2015 Towards more accurate and reliable predictions for nuclear applications. *Eur. Phys. J. A* **51**, 22. (doi:10.1140/epja/i2015-15172-2)
138. Abbott BP *et al.* 2017 Upper limits on the stochastic gravitational-wave background from advanced LIGO's first observing run. *Phys. Rev. Lett.* **118**, 161101. (doi:10.1103/PhysRevLett.118.121101)
139. Cowperthwaite PS *et al.* 2017 The electromagnetic counterpart of the binary neutron star merger LIGO/Virgo GW170817. II. UV, optical, and near-infrared light curves and comparison to kilonova models. *Astrophys. J.* **848**, L17. (doi:10.3847/2041-8213/aa8fc7)
140. Martínez-Pinedo G *et al.* 2007 The role of fission in the r-process. *Prog. Part. Nucl. Phys.* **59**, 199–205. (doi:10.1016/j.ppnp.2007.01.018)
141. Möller P, Sierk AJ, Ichikawa T, Iwamoto A, Mumpower M. 2015 Fission barriers at the end of the chart of the nuclides. *Phys. Rev. C* **91**, 024310. (doi:10.1103/PhysRevC.91.024310)
142. Panov IV, Korneev IYu, Rauscher T, Martínez-Pinedo G, Kelić-Heil A, Zinner NT, Thielemann FK. 2010 Neutron-induced astrophysical reaction rates for translead nuclei. *Astron. Astrophys.* **513**, A61. (doi:10.1051/0004-6361/200911967)
143. Vassh N *et al.* 2019 Using excitation-energy dependent fission yields to identify key fissioning nuclei in*r*-process nucleosynthesis. *J. Phys.* **46**, 065202. (doi:10.1088/1361-6471/ab0bea)
144. Wolf RN *et al.* 2013 Plumbing neutron stars to new depths with the binding energy of the exotic nuclide 82Zn. *Phys. Rev. Lett.* **110**, 242502. (doi:10.1103/PhysRevLett.110.041101)
145. Zhi Q, Caurier E, Cuenca-García JJ, Langanke K, Martínez-Pinedo G, Sieja K. 2013 Shell-model half-lives including first-forbidden contributions forr-process waiting-point nuclei. *Phys. Rev. C* **87**, 025803. (doi:10.1103/PhysRevC.87.025803)
146. Wu MR, Barnes J, Martínez-Pinedo G, Metzger BD. 2019 Fingerprints of heavy-element nucleosynthesis in the late-time lightcurves of kilonovae. *Phys. Rev. Lett.* **122**, 062701. (doi:10.1103/PhysRevLett.122.062701)
147. Möller P, Madland DG, Sierk AJ, Iwamoto A. 2001 Nuclear fission modes and fragment mass asymmetries in a five-dimensional deformation space. *Nat. New Biol.* **409**, 785–790. (doi:10.1038/35057204)
148. Schmidt KH *et al.* 2000 Relativistic radioactive beams: a new access to nuclear-fission studies. *Nucl. Phys. A* **665**, 221–267. (doi:10.1016/S0375-9474(99)00384-X)
149. Rodríguez-Sánchez JL. 2015 Complete characterization of the fission fragments produced in reactions induced by ^{208}Pb projectiles on proton at 500AMeV. *Phys. Rev. C* **91**, 064616. (doi:10.1103/PhysRevC.91.064616)

150. Graves SA, Ellison PA, Valdovinos HF, Barnhart TE, Nickles RJ, Engle JW. 2017 Half-life of ^{51}Mn. *Phys. Rev. C* **96**, 054603. (doi:10.1103/physrevc.96.014613)
151. Weber J, Britt HC, Gavron A, Konecny E, Wilhelmy JB. 1976 Fission of Ra228. *Phys. Rev. C* **13**, 2413–2420. (doi:10.1103/PhysRevC.13.2413)
152. Lang W, Clerc HG, Wohlfarth H, Schrader H, Schmidt KH. 1980 Nuclear charge and mass yields for ^{235}U(nth, f) as a function of the kinetic energy of the fission products. *Nucl. Phys. A* **345**, 34–71. (doi:10.1016/0375-9474(80)90411-X)
153. Britt HC, Hoffman DC, van der Plicht J, Wilhelmy JB, Cheifetz E, Dupzyk RJ, Lougheed RW. 1984 Fission of Es-255, Es-256, Fm-255–257, and Md-258 at moderate excitation energies. *Phys. Rev. C* **30**, 559–565. (doi:10.1103/PhysRevC.30.559)
154. Itkis M *et al.* 1988 Symmetric and asymmetric fission of nuclei lighter than thorium. *Sov. J. Part. Nucl. Phys.* **19**, 301.
155. Balantekin AB *et al.* 2020 Nonfuel antineutrino contributions in the high flux isotope reactor. *Phys. Rev. C* **101**, 054611. (doi:10.1103/PhysRevC.101.054605)
156. Jach T, Vinson J. 2022 Method for the definitive detection of orbital angular momentum states in neutrons by spin-polarized ^{3}He. *Phys. Rev. C* **105**, 064614. (doi:10.1103/PhysRevC.105.L061601)
157. Chatillon A *et al.* 2019 Experimental study of nuclear fission along the thorium isotopic chain: from asymmetric to symmetric fission. *Phys. Rev. C* **99**, 054628. (doi:10.1103/PhysRevC.99.054628)
158. Martin JF *et al.* 2021 Fission-fragment yields and prompt-neutron multiplicity for Coulomb-induced fission of ^{234,235}U and ^{237,238}Np. *Phys. Rev. C* **104**, 044602. (doi:10.1103/PhysRevC.104.044602)
159. Jach T, Vinson J. 2022 Method for the definitive detection of orbital angular momentum states in neutrons by spin-polarized ^{3}He. *Phys. Rev. C* **105**, 024618. (doi:10.1103/PhysRevC.105.L061601)
160. Andreyev AN, Huyse M, Van Duppen P. 2013 *Colloquium*: beta-delayed fission of atomic nuclei. *Rev. Mod. Phys.* **85**, 1541–1559. (doi:10.1103/RevModPhys.85.1541)
161. Ghys L *et al.* 2014 Evolution of fission-fragment mass distributions in the neutron-deficient lead region. *Phys. Rev. C* **90**, 041301. (doi:10.1103/PhysRevC.90.041301)
162. Caamaño M *et al.* 2013 Isotopic yield distributions of transfer- and fusion-induced fission from238U+12C reactions in inverse kinematics. *Phys. Rev. C* **88**, 024605. (doi:10.1103/PhysRevC.88.024605)
163. Nishio K *et al.* 2015 Excitation energy dependence of fragment-mass distributions from fission of ^{180,190}Hg formed in fusion reactions of ^{36}Ar + ^{144,154}Sm. *Phys. Lett. B* **748**, 89–94. (doi:10.1016/j.physletb.2015.06.068)
164. Pommé S *et al.* 2016 Evidence against solar influence on nuclear decay constants. *Phys. Lett. B* **761**, 281–286. (doi:10.1016/j.physletb.2016.08.038)
165. Hirose K *et al.* 2017 Role of multichance fission in the description of fission-fragment mass distributions at high energies. *Phys. Rev. Lett.* **119**, 222501. (doi:10.1103/PhysRevLett.119.222501)
166. Dulay MT, Zaman N, Jaramillo D, Mody AC, Zare RN. 2018 Pathogen-imprinted organosiloxane polymers as selective biosensors for the detection of targeted *E. coli*. *C. (Basel)*. **4**, 29. (doi:10.3390/c4020029)
167. Ramos D *et al.* 2019 Insight into excitation energy and structure effects in fission from isotopic information in fission yields. *Phys. Rev. C* **99**, 024615. (doi:10.1103/PhysRevC.99.024615)
168. Balantekin AB *et al.* 2020 Nonfuel antineutrino contributions in the high flux isotope reactor. *Phys. Rev. C* **101**, 054610. (doi:10.1103/PhysRevC.101.054605)
169. Huang WJ, Wang M, Kondev FG, Audi G, Naimi S. 2021 The AME 2020 atomic mass evaluation (I). Evaluation of input data, and adjustment procedures*. *Chin. Phys. C* **45**, 030002. (doi:10.1088/1674-1137/abddb0)
170. Rodríguez-Sánchez JL. 2014 Proton-induced fission cross sections on ^{208}Pb at high kinetic energies. *Phys. Rev. C* **90**, 064606. (doi:10.1103/PhysRevC.90.064606)
171. Rodríguez-Sánchez JL *et al.* 2015 Constraining the level density using fission of lead projectiles. *Phys. Rev. C* **92**, 044612. (doi:10.1103/PhysRevC.92.044612)

172. Meshik AP, Pravdivtseva OV, Hohenberg CM. 2016 New evidence for chemical fractionation of radioactive xenon precursors in fission chains. *Phys. Rev. C* **93**, 034605. (doi:10.1103/PhysRevC.93.044614)
173. Meshik AP, Pravdivtseva OV, Hohenberg CM. 2016 New evidence for chemical fractionation of radioactive xenon precursors in fission chains. *Phys. Rev. C* **93**, 061601((doi:10.1103/PhysRevC.93.044614)
174. Chatillon A *et al.* 2020 Evidence for a new compact symmetric fission mode in light thorium isotopes. *Phys. Rev. Lett.* **124**, 202502. (doi:10.1103/PhysRevLett.124.202502)
175. Möller P, Randrup J. 2015 Calculated fission-fragment yield systematics in the region $74 \leq Z \leq 94$ and $90 \leq N \leq 150$. *Phys. Rev. C.* **91**, 044316. (doi:10.1103/PhysRevC.91.044316)
176. Bertulani CA, Kucuk Y, Lozeva R. 2020 Fission of relativistic nuclei with fragment excitation and reorientation. *Phys. Rev. Lett.* **124**, 132301. (doi:10.1103/PhysRevLett.124.132301)
177. García-Jiménez G *et al.* 2023 Study of (p,2p) fission reactions in inverse kinematics using the R3B set-up. *EPJ. Web. Conf.* **290**, 02009. (doi:10.1051/epjconf/202329002009)
178. Balantekin AB *et al.* 2020 Nonfuel antineutrino contributions in the high flux isotope reactor. *Phys. Rev. C* **101**, 054607. (doi:10.1103/PhysRevC.101.054605)
179. Santra S *et al.* 2023 Shell effect on fission fragment mass distribution at Ecn*up to 70 MeV: role of multichance fission. *Phys. Rev. C* **107**, L061601. (doi:10.1103/PhysRevC.107.L061601)
180. Caamaño M, Rejmund F, Schmidt KH. 2011 Evidence for the predominant influence of the asymmetry degree of freedom on the even–odd structure in fission-fragment yields. *J. Phys. G: Nucl. Part. Phys.* **38**, 035101. (doi:10.1088/0954-3899/38/3/035101)
181. Geppert-Kleinrath V *et al.* 2019 Fission fragment angular anisotropy in neutron-induced fission of U235 measured with a time projection chamber. *Phys. Rev. C.* **99**, 064619. (doi:10.1103/PhysRevC.99.064619)
182. Tarrío D *et al.* 2023 Neutron-induced fission cross sections of Th232 and U233 up to 1 GeV using parallel plate avalanche counters at the CERN n_TOF facility. *Phys. Rev. C.* **107**, 044616. (doi:10.1103/PhysRevC.107.044616)
183. Rodríguez-Tajes C *et al.* 2014 Transfer reactions in inverse kinematics: an experimental approach for fission investigations. *Phys. Rev. C.* **89**, 024614. (doi:10.1103/PhysRevC.89.024614)
184. Bennett SA *et al.* 2023 Direct determination of fission-barrier heights using light-ion transfer in inverse kinematics. *Phys. Rev. Lett.* **130**, 202501. (doi:10.1103/PhysRevLett.130.202501)
185. Möller P. 2023 The most important theoretical developments leading to the current understanding of heavy-element stability. *Eur. Phys. J. A.* **59**, 77. (doi:10.1140/epja/s10050-023-00913-z)
186. Lemaître JF, Goriely S, Bauswein A, Janka HT. 2021 Fission fragment distributions and their impact on r-process nucleosynthesis in neutron star mergers. *Phys. Rev. C* **103**, 025806. (doi:10.1103/PhysRevC.103.025806)
187. Pfützner M *et al.* 1998 New isotopes and isomers produced by the fragmentation of U at 1000 MeV/nucleon. *Phys. Lett. B* **444**, 32–37. (doi:10.1016/S0370-2693(98)01332-X)
188. Podolyák Zs *et al.* 2006 High angular momentum states populated in fragmentation reactions. *Phys. Lett. B* **632**, 203–206. (doi:10.1016/j.physletb.2005.10.070)
189. Jungclaus A *et al.* 2007 Observation of isomeric decays in the r-process waiting-point nucleus 130Cd82. *Phys. Rev. Lett.* **99**, 132501. (doi:10.1103/PhysRevLett.99.132501)
190. Goldhaber AS. 1974 Statistical models of fragmentation processes. *Phys. Lett. B* **53**, 306–308. (doi:10.1016/0370-2693(74)90388-8)
191. Dudkin VE, Kovalev EE, Nefedov NA, Antonchik VA, Bogdanov SD, Ostroumov VI, Benton EV, Crawford HJ. 1991 Target fragments in collisions of 1.8 GeV/nucleon ^{56}Fe nuclei with photoemulsion nuclei, and the cascade-evaporation model. *Nucl. Phys. A* **530**, 759–769. (doi:10.1016/0375-9474(91)90778-5)
192. Pal S, Palit R. 2008 Angular momentum population in fragmentation reactions. *Phys. Lett. B* **665**, 164–167. (doi:10.1016/j.physletb.2008.06.040)
193. Graves SA, Ellison PA, Valdovinos HF, Barnhart TE, Nickles RJ, Engle JW. 2017 Half-life of ^{51}Mn. *Phys. Rev. C* **96**, 014610. (doi:10.1103/physrevc.96.014613)

194. Rodríguez-Sánchez JL *et al.* 2023 Fragmentation-induced fission reactions of ^{236}U in inverse kinematics to investigate the pre-fragment angular momentum parameterizations. *EPJ Web Conf.* **290**, 02016. (doi:10.1051/epjconf/202329002016)
195. Ohm H *et al.* 1997 Λ-hyperon lifetime in very heavy hypernuclei produced in thep+U interaction. *Phys. Rev. C* **55**, 3062–3065. (doi:10.1103/PhysRevC.55.3062)
196. Kulessa P *et al.* 1998 Production of heavy hypernuclei in the p+Bi reaction and determination of their lifetime for fission induced by Λ decay. *Phys. Lett. B* **427**, 403–408. (doi:10.1016/S0370-2693(98)00397-9)
197. Rodríguez-Sánchez JL, Cugnon J, David JC, Hirtz J, Kelić-Heil A, Vidaña I. 2023 Constraint of the nuclear dissipation coefficient in fission of hypernuclei. *Phys. Rev. Lett.* **130**, 132501. (doi:10.1103/PhysRevLett.130.132501)
198. Burgio GF, Schulze HJ, Vidaña I, Wei JB. 2021 Neutron stars and the nuclear equation of state. *Prog. Part. Nucl. Phys.* **120**, 103879. (doi:10.1016/j.ppnp.2021.103879)
199. Hebeler K, Lattimer JM, Pethick CJ, Schwenk A. 2013 Equation of state and neutron star properties constrained by nuclear physics and observation. *Astrophys. J.* **773**, 11. (doi:10.1088/0004-637X/773/1/11)
200. Huth S *et al.* 2022 Constraining neutron-star matter with microscopic and macroscopic collisions. *Nat. New Biol.* **606**, 276–280. (doi:10.1038/s41586-022-04750-w)
201. Li BA, Cai BJ, Xie WJ, Zhang NB. 2021 Progress in constraining nuclear symmetry energy using neutron star observables since GW170817. *Universe* **7**, 182. (doi:10.3390/universe7060182)
202. Navin A *et al.* 2000 Direct evidence for the breakdown of the N = 8 shell closure in ^{12}Be. *Phys. Rev. Lett.* **85**, 266–269. (doi:10.1103/PhysRevLett.85.266)
203. Typel S, Brown BA. 2001 Neutron radii and the neutron equation of state in relativistic models. *Phys. Rev. C* **64**, 027302. (doi:10.1103/PhysRevC.64.027302)
204. Roca-Maza X, Brenna M, Colò G, Centelles M, Viñas X, Agrawal BK, Paar N, Vretenar D, Piekarewicz J. 2013 Electric dipole polarizability in ^{208}Pb: insights from the droplet model. *Phys. Rev. C* **88**, 024316. (doi:10.1103/PhysRevC.88.024316)
205. Adhikari D *et al.* 2021 Accurate determination of the neutron skin thickness of ^{208}Pb through parity-violation in electron scattering. *Phys. Rev. Lett.* **126**, 172502. (doi:10.1103/PhysRevLett.126.172502)
206. Adhikari D *et al.* 2021 Accurate determination of the neutron skin thickness of ^{208}Pb through parity-violation in electron scattering. *Phys. Rev. Lett.* **126**, 172503. (doi:10.1103/PhysRevLett.126.172502)
207. Adhikari D *et al.* 2022 New measurements of the beam-normal single spin asymmetry in elastic electron scattering over a range of spin-0 nuclei. *Phys. Rev. Lett.* **128**, 042501. (doi:10.1103/PhysRevLett.128.142501)
208. Reinhard PG, Roca-Maza X, Nazarewicz W. 2022 Combined theoretical analysis of the parity-violating asymmetry for ^{48}Ca and ^{208}Pb. *Phys. Rev. Lett.* **129**, 232501. (doi:10.1103/PhysRevLett.129.232501)
209. Baliraine FW *et al.* 2024 Complete genome sequences and characteristics of mycobacteriophages Diminimus, Dulcita, Glaske16, and Koreni. *Microbiol. Resour. Announc.* **13**, e0101023. (doi:10.1128/MRA.01010-23)
210. Tamii A *et al.* 2011 Complete electric dipole response and the neutron skin in ^{208}Pb. *Phys. Rev. Lett.* **107**, 062502. (doi:10.1103/PhysRevLett.107.062502)
211. Roca-Maza X, Viñas X, Centelles M, Agrawal BK, Colò G, Paar N, Piekarewicz J, Vretenar D. 2015 Neutron skin thickness from the measured electric dipole polarizability in ^{68}Ni,^{120}Sn, and ^{208}Pb. *Phys. Rev. C* **92**, 064304. (doi:10.1103/PhysRevC.92.064304)
212. Typel S, Röpke G, Klähn T, Blaschke D, Wolter HH. 2010 Composition and thermodynamics of nuclear matter with light clusters. *Phys. Rev. C* **81**, 015803. (doi:10.1103/PhysRevC.81.015803)
213. AumannT *et al.* 2020 . Constraining energy-density functionals and the density-dependence of the symmetry energy bymeasurements of accurate cross sections with large acceptance at R3B. G-PAC proposal. S515.
214. Li B, Chen L, Ko C. 2008 Recent progress and new challenges in isospin physics with heavy-ion reactions. *Phys. Rep.* **464**, 113–281. (doi:10.1016/j.physrep.2008.04.005)

215. Fèvre AL *et al.* 2022 Symmetry energy at high densities from neutron/proton flow excitation function. G-PAC proposal
216. Meshik AP, Pravdivtseva OV, Hohenberg CM. 2016 New evidence for chemical fractionation of radioactive xenon precursors in fission chains. *Phys. Rev. C* **93**, 034608. (doi:10.1103/PhysRevC.93.044614)
217. Particle data group prog. 2020 Review of particle physics. *Theor. Exp. Phys.* **8**, 083C01. (doi:10.1093/ptep/ptaa104)
218. Danysz M, Pniewski J. 1953 Delayed disintegration of a heavy nuclear fragment: I. *The Lond. Edinb. and Dub. Philos. Mag. J. Sci.* **44**, 348–350. (doi:10.1080/14786440308520318)
219. Petschauer S, Haidenbauer J, Kaiser N, Meißner UG, Weise W. 2020 Hyperon-nuclear interactions from SU(3) chiral effective field theory. *Front. Phys.* **8**. (doi:10.3389/fphy.2020.00012)
220. Hashimoto O, Tamura H. 2006 Spectroscopy of Λ hypernuclei. *Prog. Part. Nucl. Phys.* **57**, 564–653. (doi:10.1016/j.ppnp.2005.07.001)
221. Gibson BF, Lehman DR. 1998 Four-body calculation of the 0+-1+ binding energy difference in the A=4 Λ hypernuclei. *Phys. Rev. C* **37**, 679. (doi:10.1103/PhysRevC.37.679)
222. Akaishi Y, Harada T, Shinmura S, Myint KS. 2000 Coherent lambda-sigma coupling in s-shell hypernuclei. *Phys. Rev. Lett.* **84**, 3539–3541. (doi:10.1103/PhysRevLett.84.3539)
223. Nakazawa K, Takahashi H. 2010 Experimental study of double-Λ hypernuclei with nuclear emulsion. *Prog. Theor. Phys. Suppl.* **185**, 335–343. (doi:10.1143/PTPS.185.335)
224. Vidaña I, Polls A, Ramos A, Engvik L, Hjorth-Jensen M. 2000 Hyperon-hyperon interactions and properties of neutron star matter. *Phys. Rev. C* **62**, 035801. (doi:10.1103/PhysRevC.62.035801)
225. Antoniadis J *et al.* 2013 A massive pulsar in A compact relativistic binary. *Science* **340**, 448. (doi:10.1126/science.1233232)
226. Lonardoni D, Lovato A, Gandolfi S, Pederiva F. 2015 Hyperon puzzle: hints from quantum Monte Carlo calculations. *Phys. Rev. Lett.* **114**, 092301. (doi:10.1103/PhysRevLett.114.092301)
227. Rayet M. 1981 Skyrme parametrization of an effective Λ-nucleon interaction. *Nucl. Phys. A* **367**, 381–397. (doi:10.1016/0375-9474(81)90655-2)
228. Motoba T, Bando H, Ikeda K. 1983 Light p-shell-hypernuclei by the microscopic three-cluster model. *Prog. Theor. Phys.* **70**, 189–221. (doi:10.1143/PTP.70.189)
229. Rufa M, Stocker H, Reinhard PG, Maruhn J, Greiner W. 1987 Single-particle spectra of Λ hypernuclei and the enhanced interaction radii of multi-strange objects. *J. Phys. G: Nucl. Phys.* **13**, L143–L148. (doi:10.1088/0305-4616/13/8/003)
230. Mares J, Zofka J. 1989 On ΛΛ hyperon(s) in the nuclear medium. *Z. Phys. A* **333**, 209.
231. Tretyakova TYu, Lanskoy DE. 1999 Structure of neutron-rich Λ hypernuclei. *Eur. Phys. J. A.* **5**, 391–398. (doi:10.1007/s100500050302)
232. Cugnon J, Lejeune A, Schulze HJ. 2000 Hypernuclei in the Skyrme-Hartree-Fock formalism with a microscopic hyperon-nucleon force. *Phys. Rev. C* **62**, 064308. (doi:10.1103/PhysRevC.62.064308)
233. Hiyama E, Yamada T. 2009 Structure of light hypernuclei. *Prog. Part. Nucl. Phys.* **63**, 339–395. (doi:10.1016/j.ppnp.2009.05.001)
234. Gal A, Soper JM, Dalitz RH. 1971 A shell-model analysis of Λ binding energies for the p-shell hypernuclei. I. Basic formulas and matrix elements for ΛN and ΛNN forces. *Ann. Phys. (N. Y.).* **63**, 53–126. (doi:10.1016/0003-4916(71)90297-1)
235. Gal A, Soper JM, Dalitz RH. 1972 A shell-model analysis of Λ binding energies for the p-shell hypernuclei II. Numerical Fitting, Interpretation, and Hypernuclear Predictions. *Ann. Phys. (N. Y.).* **72**, 445–488. (doi:10.1016/0003-4916(72)90222-9)
236. Gal A, Soper JM, Dalitz RH. 1978 A shell-model analysis of Λ binding energies for the p-shell hypernuclei III. Further analysis and predictions. *Ann. Phys. (N. Y.).* **113**, 79–97. (doi:10.1016/0003-4916(78)90250-6)
237. Nucl DJ. 2008 Shell-model interpretation of gamma-ray transitions in p-shell hypernuclei. *Phys. A.* **804**, 84. (doi:10.1016/j.nuclphysa.2008.02.252)
238. Nucl DJ. 2010 Graphical Abstract: ChemBioChem 7/2010. *Chembiochem* **11**, 835–842. (doi:10.1002/cbic.201090027)
239. Millener DJ. 2012 Shell-model calculations for p-shell hypernuclei. *Nucl. Phys. A* **881**, 298–309. (doi:10.1016/j.nuclphysa.2012.01.019)

240. Wirth R, Gazda D, Navrátil P, Calci A, Langhammer J, Roth R. 2014 Ab initio description of p-shell hypernuclei. *Phys. Rev. Lett.* **113**, 192502. (doi:10.1103/PhysRevLett.113.192502)
241. Wirth R, Roth R. 2016 Induced hyperon-nucleon-nucleon interactions and the hyperon puzzle. *Phys. Rev. Lett.* **117**, 182501. (doi:10.1103/PhysRevLett.117.182501)
242. Wirth R, Roth R. 2018 Light neutron-rich hypernuclei from the importance-truncated no-core shell model. *Phys. Lett. B.* **779**, 336–341. (doi:10.1016/j.physletb.2018.02.021)
243. Wirth R, Gazda D, Navrátil P, Roth R. 2018 Hypernuclear no-core shell model. *Phys. Rev. C* **97**, 064315. (doi:10.1103/PhysRevC.97.064315)
244. Lonardoni D, Gandolfi S, Pederiva F. 2013 Effects of the two-body and three-body hyperon-nucleon interactions inΛhypernuclei. *Phys. Rev. C.* **87**, 041303. (doi:10.1103/PhysRevC.87.041303)
245. Lonardoni D, Pederiva F, Gandolfi S. 2014 Accurate determination of the interaction between Λ hyperons and nucleons from auxiliary field diffusion Monte Carlo calculations. *Phys. Rev. C.* **89**, 014314. (doi:10.1103/PhysRevC.89.014314)
246. Khan E, Margueron J, Gulminelli F, Raduta AR. 2015 Microscopic evaluation of the hypernuclear chart with Λ hyperons. *Phys. Rev. C.* **92**, 044313. (doi:10.1103/PhysRevC.92.044313)
247. ALICE collaboration. 2022 Measurement of the lifetime and Λ separation energy of 3ΛH (doi:10.48550/arXiv.2209.07360)
248. Abdallah MS *et al.* 2022 Measurements of 3ΛH and 4ΛH lifetimes and yields in Au+Au collisions in the high Baryon density region. *Rev. Lett.* **128**, 202301. (doi:10.1103/PhysRevLett.128.202301)
249. Acharya S *et al.* 2018 D-Meson azimuthal anisotropy in midcentral Pb-Pb collisions at $\sqrt{s_{NN}}$ = 5.02TeV. *Phys. Rev. Lett.* **120**, 321. (doi:10.1103/PhysRevLett.120.102301)
250. Nield KJ, Bowen T, Cable GD, DeLise DA, Jenkins EW, Kalbach RM, Noggle RC, Pifer AE. 1976 Production of hypernuclei in a 2.1 GeV/nucleon oxygen beam. *Phys. Rev. C* **13**, 1263–1266. (doi:10.1103/PhysRevC.13.1263)
251. Avramenko S *et al.* 1992 A study of the production and lifetime of the lightest relativistic hypernuclei. *Nucl. Phys. A* **547**, 95–100. (doi:10.1016/0375-9474(92)90714-U)
252. Saito TR *et al.* 2016 Summary of the HypHI Phase 0 experiment and future plans with FRS at GSI (FAIR Phase 0). *Nucl. Phys. A* **954**, 199–212. (doi:10.1016/j.nuclphysa.2016.05.011)
253. Saito TR *et al.* 2021 New directions in hypernuclear physics. *Nat. Rev. Phys.* **3**, 803–813. (doi:10.1038/s42254-021-00371-w)
254. Saito TR, Ekawa H, Nakagawa M. 2021 Novel method for producing very-neutron-rich hypernuclei via charge-exchange reactions with heavy ion projectiles. *Eur. Phys. J. A* **57**, 159. (doi:10.1140/epja/s10050-021-00470-3)
255. Obertelli A *et al.* 2022 Matter radius of the hyperhalo candidate 3ΛH from interaction cross-section measurements. G-PAC proposal S073
256. Jurič M *et al.* 1973 A new determination of the binding-energy values of the light hypernuclei (A ⩽ 15). *Nucl. Phys. B* **52**, 1. (doi:10.1016/0550-3213(73)90084-9)
257. Trogolo S. 2019 Addressing the hypertriton lifetime puzzle with ALICE at the LHC. *Nucl. Phys. A* **982**, 815–818. (doi:10.1016/j.nuclphysa.2018.11.016)
258. Hiyama E, Kamimura M, Motoba T, Yamada T, Yamamoto Y. 1996 Three-body model study of *A*=6–7 hypernuclei: Halo and skin structures. *Phys. Rev. C* **53**, 2075–2085. (doi:10.1103/PhysRevC.53.2075)
259. Knöll M, Roth R. 2023 Hyperon-nucleon interaction constrained by light hypernuclei (doi:10.48550/arXiv.2307.11577)
260. Gebrerufael E, Vobig K, Hergert H, Roth R. 2017 AbInitio description of open-shell nuclei: merging no-core shell model and in-medium similarity renormalization group. *Phys. Rev. Lett.* **118**, 152503. (doi:10.1103/PhysRevLett.118.152503)
261. Botvina AS, Steinheimer J, Bratkovskaya E, Bleicher M, Pochodzalla J. 2015 Formation of hypermatter and hypernuclei within transport models in relativistic ion collisions. *Phys. Lett. B* **742**, 7–14. (doi:10.1016/j.physletb.2014.12.060)
262. Dulay MT, Zaman N, Jaramillo D, Mody AC, Zare RN. 2018 Pathogen-imprinted organosiloxane polymers as selective biosensors for the detection of targeted *E. coli*. *C. (Basel).* **4**, 29. (doi:10.3390/c4020029)

263. Graves SA, Ellison PA, Valdovinos HF, Barnhart TE, Nickles RJ, Engle JW. 2017 Half-life of ^{51}Mn. *Phys. Rev. C* **96**, 034617. (doi:10.1103/physrevc.96.014613)
264. Suda T, Prog H. 2017 Prospects for electron scattering on unstable, exotic nuclei. *Nucl. Phys.* **96**, 1. (doi:10.1016/j.ppnp.2017.04.002)
265. Wakasugi M *et al.* 2008 Novel internal target for electron scattering off unstable nuclei. *Phys. Rev. Lett.* **100**, 164801. (doi:10.1103/PhysRevLett.100.164801)
266. Tsukada K *et al.* 2017 First elastic electron scattering from ^{132}Xe at the SCRIT facility. *Phys. Rev. Lett.* **118**, 262501. (doi:10.1103/PhysRevLett.118.262501)
267. Tsukada K *et al.* 2023 First observation of electron scattering from online-produced radioactive target. *Phys. Rev. Lett.* **131**, 092502. (doi:10.1103/PhysRevLett.131.092502)
268. Antonov AN *et al.* 2011 The electron–ion scattering experiment ELISe at the International Facility for Antiproton and Ion Research (FAIR)—A conceptual design study. *Nucl. Instrum. Methods A* **637**, 60–76. (doi:10.1016/j.nima.2010.12.246)
269. Frankfurt L *et al.* 2020 Review of opportunities at the HESR-Collider with PANDA at FAIR (doi:10.48550/arXiv.1908.02346)
270. Most ER, Motornenko A, Steinheimer J, Dexheimer V, Hanauske M, Rezzolla L, Stoecker H. 2023 Probing neutron-star matter in the lab: similarities and differences between binary mergers and heavy-ion collisions. *Phys. Rev. D* **107**, 043034. (doi:10.1103/PhysRevD.107.043034)
271. Blacker S, Bauswein A, Typel S. 2023 Exploring thermal effects of the hadron-quark matter transition in neutron star mergers. *Phys. Rev. D* **108**, 063032. (doi:10.1103/PhysRevD.108.063032)
272. Adamczewski-Musch J *et al.* 2023 Proton, deuteron and triton flow measurements in Au+Au collisions at $\sqrt{S_{NN}}$ = 2.4 GeV. *Eur. Phys. J. A* **59**, 80. (doi:10.1140/epja/s10050-023-00936-6)
273. Abou Yassine R *et al.* 2022 Measurement of global polarization of Λ hyperons in few-GeV heavy-ion collisions. *Phys. Lett. B* **835**, 137506. (doi:10.1016/j.physletb.2022.137506)
274. Adamczewski-Musch J *et al.* 2020 Directed, elliptic, and higher order flow harmonics of protons, deuterons, and tritons in Au+Au collisions at $\sqrt{S_{NN}}$ = 2.4 GeV. *Phys. Rev. Lett.* **125**, 262301. (doi:10.1103/PhysRevLett.125.262301)
275. Assari S, Boyce S, Bazargan M, Caldwell CH, Mincy R. 2020 Maternal education at birth and youth breakfast consumption at age 15: blacks' diminished returns. *J. (Basel).* **3**, 313–323. (doi:10.3390/j3030024)
276. Balantekin AB *et al.* 2020 Nonfuel antineutrino contributions in the high flux isotope reactor. *Phys. Rev. C* **101**, 024914. (doi:10.1103/PhysRevC.101.054605)
277. Adamczewski-Musch J *et al.* 2019 Probing dense baryon-rich matter with virtual photons. *Nat. Phys.* **15**, 1040–1045. (doi:10.1038/s41567-019-0583-8)
278. Leifels Y *et al.* 2019 Sub-threshold production of Ks0mesons and Λ hyperons in Au+Au collisions atsNN=2.4GeV. *Phys. Lett. B* **793**, 457–463. (doi:10.1016/j.physletb.2019.03.065)
279. Dulay MT, Zaman N, Jaramillo D, Mody AC, Zare RN. 2018 Pathogen-imprinted organosiloxane polymers as selective biosensors for the detection of targeted *E. coli*. *C. (Basel).* **4**, 29. (doi:10.3390/c4020029)
280. Li BA *et al.* 2008 Recent progress and new challenges in isospin physics with heavy-ion reactions. *Phys. Rep.* **464**, 113. (doi:10.1016/j.physrep.2008.04.005)
281. Jhang G *et al.* 2021 Symmetry energy investigation with pion production from Sn+Sn systems. *Phys. Lett. B* **813**, 136016. (doi:10.1016/j.physletb.2020.136016)
282. Colonna M. 2020 Collision dynamics at medium and relativistic energies. *Prog. Part. Nucl. Phys.* **113**, 103775. (doi:10.1016/j.ppnp.2020.103775)
283. Li BA, Chen LW, Ko CM. 2008 Recent progress and new challenges in isospin physics with heavy-ion reactions. *Phys. Rep.* **464**, 113–281. (doi:10.1016/j.physrep.2008.04.005)
284. Sorensen A *et al.* 2024 Dense nuclear matter equation of state from heavy-ion collisions. *Prog. Part. Nucl. Phys.* **134**, 104080. (doi:10.1016/j.ppnp.2023.104080)
285. Hombach A, Cassing W, Mosel U. 1999 Isospin equilibration in relativistic heavy-ion collisions. *EPJ A* **5**, 77–84. (doi:10.1007/s100500050259)
286. Di Toro M *et al.* 2009 Isospin dynamics in heavy ion collisions: from Coulomb barrier to quark gluon plasma. *Prog. Part. Nucl. Phys.* **62**, 389–401. (doi:10.1016/j.ppnp.2008.12.038)

287. Dolinskii A *et al.* 2015 Collector ring project at FAIR. *Phys. Scr.* **T166**, 014040. (doi:10.1088/0031-8949/2015/T166/014040)